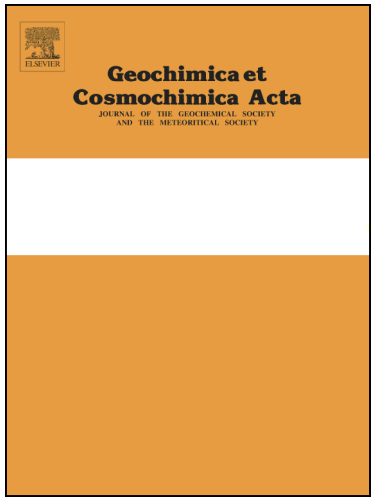

The coupled geochemistry of Au and As in pyrite from hydrothermal ore deposits

Artur P. Deditius, Martin Reich, Stephen E. Kesler, Satoshi Utsunomiya, Stephen L. Chryssoulis, John Walshe, Rodney C. Ewing

PII: S0016-7037(14)00392-5
DOI: http://dx.doi.org/10.1016/j.gca.2014.05.045
Reference: GCA 8847

To appear in: *Geochimica et Cosmochimica Acta*

Received Date: 3 February 2014
Accepted Date: 26 May 2014

Please cite this article as: Deditius, A.P., Reich, M., Kesler, S.E., Utsunomiya, S., Chryssoulis, S.L., Walshe, J., Ewing, R.C., The coupled geochemistry of Au and As in pyrite from hydrothermal ore deposits, *Geochimica et Cosmochimica Acta* (2014), doi: http://dx.doi.org/10.1016/j.gca.2014.05.045

Submitted to Geochimica et Cosmochimica Acta

May 22, 2014

The coupled geochemistry of Au and As in pyrite from hydrothermal ore deposits

Artur P. Deditius[1], Martin Reich[2,3], Stephen E. Kesler[4], Satoshi Utsunomiya[5], Stephen L. Chryssoulis[6], John Walshe[7], Rodney C. Ewing[4]

[1]*Murdoch University, School of Veterinary and Life Sciences, 90 South Street, Murdoch, Western Australia 6150, Australia*

[2]*Department of Geology, Universidad de Chile, Santiago, Chile*

[3]*Andean Geothermal Center of Excellence, Universidad de Chile, Santiago, Chile*

[4]*Department of Earth and Environmental Sciences, University of Michigan, 1100 N. University Ave., Ann Arbor, MI 48509-1005, USA*

[5]*Department of Chemistry, Kyushu University, Ropponmatsu 4-2-1, Chuo-ku, Fukuoka-Shi, 810-8560, Japan*

[6]*Advanced Mineral Technology Laboratory (AMTEL), 100 Collip Circle, UWO Research Park, London, ON, Canada N6G 4X8*

[7]*CSIRO, Earth Science and Resource Engineering, 26 Dick Perry Avenue, Kensington, WA 6151, Australia*

Corresponding author:

Artur P. Deditius

School of Engineering and Information Technology,

Murdoch University

Western Australia 6150, Australia

E-mail: A.Deditius@murdoch.edu.au; Tel.: +61 8 9360 2525.

Abstract

The ubiquity of Au-bearing arsenian pyrite in hydrothermal ore deposits suggests that the coupled geochemical behaviour of Au and As in this sulfide occurs under a wide range of physico-chemical conditions. Despite significant advances in the last 20 years, fundamental factors controlling Au and As ratios in pyrite from ore deposits remain poorly known. Here we explore these constraints using new and previously published EMPA, LA-ICP-MS, SIMS, and μ-PIXE analyses of As and Au in pyrite from Carlin-type Au, epithermal Au, porphyry Cu, Cu-Au, and orogenic Au deposits, volcanogenic massive sulfide (VHMS), Witwatersrand Au, iron oxide copper gold (IOCG), and coal deposits. Pyrite included in the data compilation formed under temperatures from ~30 ^{o}C to ~600 ^{o}C and in a wide variety of geological environments. The pyrite Au-As data form a wedge-shaped zone in compositional space, and the fact that most data points plot below the solid solubility limit defined by Reich et al. (2005) indicate that Au^{1+} is the dominant form of Au in arsenian pyrite and that Au-bearing ore fluids that deposit this sulfide are mostly undersaturated with respect to native Au. The analytical data also show that the solid solubility limit of Au in arsenian pyrite defined by an Au/As ratio of 0.02 is independent of the geochemical environment of pyrite formation and rather depends on the crystal-chemical properties of pyrite and post-depositional alteration. Compilation of Au-As concentrations and formation temperatures for pyrite indicates that Au and As solubility in pyrite is retrograde; Au and As contents decrease as a function of increasing temperature from ~200 ^{o}C to ~500 ^{o}C. Based on these results, two major Au-As trends for Au-bearing arsenian pyrite from ore deposits are defined. One trend

is formed by pyrites from Carlin-type and orogenic Au deposits where compositions are largely controlled by fluid-rock-interactions and/or can be highly perturbed by changes in temperature and alteration by hydrothermal fluids. The second trend consists of pyrites from porphyry Cu and epithermal Au deposits, which are characterized by compositions that preserve the Au/As signature of mineralizing magmatic-hydrothermal fluids, confirming the role of this sulfide in controlling metal ratios in ore systems.

1. INTRODUCTION

Pyrite is the most common sulfide in the Earth's crust. It is important to ore deposits and environmental geochemistry because it hosts economically valuable amounts of Au associated with other metals and metalloids that can be enriched up to the weight percent (wt. %) level, including As, Hg, and Tl (e.g., Arehart et al., 1993; Cook and Chryssoulis, 1990; Chowdhurry et al., 1999; Hofstra and Cline, 2000; Smedley and Kinniburgh, 2002; Goldfarb et al., 2005; Reich et al., 2005; Seedorff et al., 2005; Simmons et al., 2005; Rickard and Luther, 2007; Large et al., 2009; Deditius et al., 2011; Reich et al., 2013). Previous studies have shown that pyrite microstructure is complex and can record valuable information about the chemical and isotopic evolution of the fluids from which it precipitates (e.g., Frimmel, 2005; Wagner and Boyce, 2006; Farquhar et al., 2007; Phillipot et al., 2007; Barker et al., 2009; Deditius et al., 2009a; Reich et al., 2013; Agangi et al., 2014; Ingham et al., 2014). Moreover, it has been shown recently that pyrite can host trace elements not only as solid solution or "structurally bound" species, but also as nanoparticles of metals with varying degrees of compositional complexity from native Au to Fe-As-Sb-Pb-Ni-Au-S nanophases (Palenik et al., 2004; Deditius et al., 2011a; Hough et al., 2012).

Gold and arsenic incorporation into pyrite is strongly coupled in pyrite from many

different types of ore deposits, including Carlin-type Au (e.g., Cline, 2001; Emsbo et al., 2003; Reich et al., 2005; Muntean et al., 2011), porphyry Cu, Cu-Au, and epithermal Au (e.g., Cook and Chryssouliss, 1990; Deditius et al., 2008; Reich et al., 2013), orogenic Au (e.g., Morey et al., 2008; Large et al., 2007), volcanogenic massive sulphide (VHMS) (Huston et al., 1995; McClenaghan et al., 2004), iron-oxide Cu-Au (IOCG) (Foster et al., 2007) and Witwatersrand modified paleoplacer Au deposits (Frimmel et al., 2005; Agangi et al., 2013). Reich et al. (2005) showed that the maximum amount of Au that can be incorporated into pyrite is mainly a function of As concentration. In addition to As content, other factors that might control Au concentration in pyrite are the temperature of formation, subsequent metamorphism and/or alteration, the amounts of other trace elements, and the size of individual grains (e.g., Mumin et al., 1994; Fleet and Mumin, 1997; McClanaghan et al., 2004; Reich et al., 2005, Reich et al., 2006; Large et al., 2007; Deditius et al., 2008, Deditius et al., 2011a; Masslennikov et al., 2009).

In this study we evaluate the role of these factors using new and previously published SIMS, LA-ICP-MS, EMPA, and μ-PIXE analyses of pyrite from Carlin-type Au, epithermal Au, porphyry Cu and Cu-Au, orogenic Au, VHMS, IOCG, Witwatersrand Au, active hydrothermal vents in submarine environments, and coal deposits. By analysing a large data set of Au-As analyses, we define the chemical limits of incorporation of Au and As in pyrite, and constrain the Au-As compositional fields for pyrite formed in different environments of ore formation. In addition, we explore the mineralogical and geochemical factors controlling Au and As speciation in pyrite, while discussing the extent to which its Au-As composition preserves the Au/As signature of parent fluids.

2. LITERATURE OVERVIEW

2.1 Arsenic solubility and speciation

Concentrations of As in pyrite vary from below detection limit (bdl) to 19 wt. % in pyrite that contains As^{1-} species (Simon et al., 1999; Reich et al., 2005), and from bdl to 5.5 wt. % in pyrite hosting As^{3+} (Deditius et al., 2008). Recently, Qian et al. (2012) synthesized arsenian pyrite that contains As^{2+} species at concentrations as high as 24 wt. %. In addition, As can occur as amorphous As-Fe-S nanoparticle aggregates in arsenian pyrite, which suggests that As^0 species can also be present (Deditius et al., 2009b).

Experimental syntheses of arsenian pyrite are very limited, and most information on thermodynamic stability and kinetics has been retrieved from textural analysis of natural samples. Fleet and Mumin (1997) suggested, based on observations of fine-grained experimental runs, that precipitation of Au-rich arsenian pyrite is a kinetically-favoured and surface-controlled phenomenon resulting in As reduction. For example, sorption of the dominant dissolved As-species $As^{3+}(OH)_3$ (Pokrovski et al., 1996) under ambient conditions results in reduction of As^{3+} to As^{1-} in the pyrite structure with local formation of a FeAsS-like precipitate (Bostick and Fendorf, 2003). Also, experimental data show that reaction paths involved in the formation of arsenian pyrite and speciation of As in its structure depend on the type or nature of the initial mineral nucleus (Fleet and Mumin, 1997; Qian et al., 2012). Hydrothermal synthesis by Fleet and Mumin (1997) between 200 and 500 ^oC resulted in anionic As^{1-} species with a maximum concentration of 7.7 wt. % when pyrite was formed by replacement of pyrrhotite. In contrast, As^{2+} incorporation is favoured when arsenian pyrite is formed via replacement of magnetite, under temperature conditions between 125 and 220 ^oC (Qian et al., 2012). Arsenic solubility in pyrite decreases with increasing temperature, and pyrite hosts only ~20-190 ppm As at ~500 ^oC and Au < 3 ppm (Tauson, 1999). First principles calculations by Reich and Becker (2006) predicted that two-phase mixtures of

pyrite (FeS_2) and arsenopyrite (FeAsS) are energetically more favorable than the solid solution $Fe(S,As)_2$ (arsenian pyrite) for a wide range of geologically relevant temperatures. Results from that study predict that pyrite can host up to ~6 wt. % As in solid solution before unmixing into a pyrite+arsenopyrite mixture of nanodomains. This feature has been reported from Carlin-type deposits where structurally distorted zones of As-rich pyrite with coexisting nanocrystalline As-pyrite, arsenopyrite and pyrrhotite surround Au nanoparticles, (Palenik et al., 2004). Recent density functional (DFT) calculations of position and correlation between Au and As in pyrite showed a decrease in the formation energy of Au-bearing pyrite with an increase in As concentration (Chen et al., 2013).

2.2 Gold solubility and speciation

Gold is present in arsenian pyrite as structurally-bound Au^{1+} or Au-bearing nanoparticles, usually native Au and/or Au tellurides (Saunders, 1990; Simon et al., 1999a; Palenik et al., 2004; Ciobanu et al., 2012); Au^{3+} incorporation has also been suggested (Arehart et al., 1993; Chouinard et al., 2005a) but to date, no spectroscopic confirmation has been reported. Substitution of anionic or cationic As into the pyrite structure enhances incorporation of Au due to structural distortion and/or decrease of the size of pyrite grains, i.e., increase of the surface/volume ratio (e.g., Palenik et al., 2004; Simon et al., 1999b; Deditius et al., 2008). Several different coupled incorporation mechanisms for Au and As have been proposed for pyrite. The most widely accepted involves the substitution of cationic Au for Fe in distorted octahedral sites and anionic As for S in tetrahedral structural sites. X-ray absorption near edge structure (XANES) and extended X-ray absorption fine structure (EXAFS) data suggest that Au in pyrite can also be coordinated by two or four S atoms (Simon et al., 1999a). In this case, the relatively large ionic radius of Au^{+} suggests that its incorporation is accompanied by

significant distortion of the pyrite structure leading to possible vacancy formation (Simon et al., 1999a). Chouinard et al. (2005a) proposed a coupled substitution mechanism of the type $Au^{3+} + Cu^{+} \Leftrightarrow 2Fe^{2+}$, to explain the incorporation of Au in pyrite samples from the Chilean Pascua Lama high-sulfidation epithermal Au deposit. According to these authors, As^{3+} substitutes for Fe^{2+} according to $Ag^{+} + As^{3+} \Leftrightarrow 2Fe^{2+}$. Alternatively, excess charge related to cationic As incorporation in pyrite has been interpreted to reflect the presence of vacancies (Deditius et al., 2008). Therefore, the incorporation of oxidized Au and As species in pyrite due to higher fO_2 conditions characteristic of high-sulfidation epithermal deposits (Simmons et al., 2005) may be accommodated by a mechanism incorporating the effect of vacancies of the type $As^{3+} + yAu^{+} + 1\text{-}y(\square) \Leftrightarrow 2Fe^{2+}$.

Highest concentrations of Au in pyrite are always related to the presence of Au-bearing micro- to nano-sized inclusions and clusters of Au nanoparticles. Examples include concentrations of 0.84 wt. % of Au at the Screamer Carlin-type deposit (Palenik et al., 2004), 1.1 wt. % of Au from the Emperor epithermal Au deposit in Fiji (Pals et al., 2003), below 800 ppm Au in the Dexing porphyry Cu deposit in southeastern China (Reich et al., 2013); and ~1.15 wt. % from the Dongping orogenic Au deposit in northern China (Cook et al., 2009).

2.3 Mechanisms of Au and As incorporation

Solid solubility of Au in arsenian pyrite was confirmed from SIMS and EMPA analyses of pyrite samples from Carlin-type and epithermal Au deposits (Reich et al., 2005). The authors defined the empirical solid solubility of Au in As-pyrite as $C_{Au} = 0.02 \times C_{As} + 4 \times 10^{-5}$ for a range of temperature between ~150-250 ^{o}C (Fig. 1, red line). At Au/As ratios above the solubility limit (Au:As = 1:200), Au is present as nanoparticles of native metal (Au^{0}), and at ratios below the solubility line, it is present as cationic Au in solid solution (Simon et al.,

1999a; Chouinard et al., 2005a; Reich et al., 2005). Arsenic, on the other hand, usually occurs in its anionic As^{1-} state in pyrite (Simon et al., 1999a; Savage et al., 2000), although recent studies have reported cationic $As^{2+,3+}$-species under oxidizing conditions typical of high-sulfidation epithermal and porphyry deposits (Deditius et al., 2008; Qian et al., 2012) (Fig. 2).

Several authors have recognized deviations from the solubility limit, particularly in orogenic/ Au deposits. Sung et al. (2009) found Au nanoparticles in pyrite plotting below the solubility limit (solid solution Au domain) in the Sunrise Dam (Western Australia) orogenic Au deposit, and Cook et al. (2009) reported relatively high concentrations of Au in As-depleted and As-"free" pyrite from orogenic Au deposits at Dongping in China. Deditius et al. (2008), on the other hand, found Au as solid solution occurring in the field of nanoparticulate Au in samples form the high-sulfidation epithermal Au deposit in Yanacocha, Peru. These anomalous behaviours of Au in arsenian pyrite were attributed to temperature of pyrite formation, kinetics and rate of growth, association of other trace elements or "proximity effects", electrochemical features of pyrite mineral surface, and speciation of Au and As in the mineralizing fluid, and in pyrite itself (Becker et al., 2001; Mikhlin et al., 2011).

Generally, it has been established that an increase in the As concentration in pyrite and formation of an Fe-deficient surface promotes incorporation of Au into solid solution (Johan et al., 1989; Fleet and Mumin, 1997; Reich et al., 2005). Fleet and Mumin (1997) proposed the incorporation mechanism for Au via chemisorption onto As-rich, Fe-deficient pyrite surface and formation of a metastable solid-solution. Such a process would proceed according to local, nano-scale equilibrium of the pyrite surface with Au-rich fluid resulting in heterogeneous distribution of Au even within a single grain of pyrite (Palenik et al., 2004). In addition, sorption of Au may be enhanced by changes in the semiconducting properties of pyrite (*n*-type to *p*-type) due to the incorporation of As (e.g., Maddox et al., 1998; Rickard and Luther, 2007). Pokrovski et al. (2002a) proposed that the surface of arsenian pyrite is

locally reducing so that it may be responsible for the destabilization of Au-sulfide complexes and Au deposition, a process that would favor rapid growth of Au-bearing arsenian pyrite under non-equilibrium conditions (Reich et al., 2005; Deditius et al., 2008; Qian et al., 2012 and references therein).

2.4 Zoning, textures and conditions of arsenian pyrite formation in major types of ore deposits

Arsenian pyrite is the main host for Au in Carlin-type Au deposits in Nevada (Arehart et al., 1993; Cline et al., 2005). "Invisible" Au concentrates in growth zones of fine-grained (< 10 μm) pyrite that also contain significant amounts of Cu, Te, Hg, Sb, and Tl (Emsbo et al., 2003; Barker et al., 2009). The Au-As-rich growth zones of pyrite precipitated on the surface of trace element-poor, pre-ore pyrite are a few nanometers to a few tens of microns thick. The pre-ore stage pyrite occurs as framboidal pyrite and/or subhedral to euhedral grains of pyrite up to 1 mm in diameter (Arehart et al., 1993; Simon et al., 1999b; Barker et al., 2009; Su et al., 2012). The growth zones of ore stage pyrite are porous and form spongy, colloform textures (Simon et al., 1999b; Palenik et al., 2004; Muntean et al., 2011). Nano-SIMS analyses and elemental maps of As-Au-bearing colloform pyrite revealed coupling of Au and As in several nanoscale growth zones. The amount of Au in arsenian pyrite in Carlin-type and epithermal deposits increases with decrease of the size of pyrite grains, although even coarse-grained arsenian pyrite contains tens of ppm Au (Simon et al., 1999b; Deditius et al., 2008).

Carlin-type deposits are thought to have been deposited from aqueous and/or aqueous-carbonic fluids that underwent phase separation during migration along fault zones in an extensional setting (Muntean et al., 2011). The Au ore was deposited due to destabilization of Au-bisulphide complexes during sulfidation of carbonate wall rocks, at shallow crustal levels.

Fluid inclusions indicate a low salinity (~2-3 wt. % $NaCl_{equiv.}$) for the mineralizing fluid with temperatures between 180-240 ^{o}C. $\delta^{34}S$ analyses of pyrite indicate a magmatic source for some sulfur, with variable contributions of sedimentary sulfur (Cline, 2001; Emsbo et al., 2003).

Textural and compositional studies of pyrite from orogenic Au deposits have revealed that single grains can show up to six different generations of pyrite with heterogeneous distribution of Au, As, and other trace elements. Similar to pyrite from Carlin-type deposits, growth zoning is a major factor controlling element distribution in pyrite in orogenic deposits. (Goldfarb et al., 2005; Large et al., 2007; Morey et al., 2008; Large et al., 2009; Sung et al., 2009; Thomas et al., 2011). The complexity of pyrite growth reflects the multi-stage evolution of orogenic Au deposits, where Au deposition is usually related to episodic pumping of fluids produced during greenschist to amphibolite facies devolatilization and that are structurally channelled into the retrograding parts of an orogen (Sibson et al., 1988; Goldfarb et al., 2005). The size of pyrite grains varies from submicron to centimetre-scale subhedral to euhedral grains. The concentrations of Au in vein-stage, hydrothermal coarse-grained pyrite are usually below 10 ppm. Gold tends to concentrate in As-rich zones and/or zones of intense brittle deformation in coarse-grained pyrite, in the relicts of framboidal pyrite (if preserved), and in areas of extensive pyrite recrystallization due to interaction with Au-bearing hydrothermal fluids. Gold content in pyrite decreases to < 1 ppm in pristine, unzoned pyrite (Ho et al., 1995; Large et al., 2007; Morey et al., 2008; Cook et al., 2009; Large et al., 2009; Sung et al., 2009; Thomas et al., 2011; Velásquez et al., 2014). Some generations of pyrite at Bendigo, Victoria, Australia, also reveal syndeformational growth marked by coupled changes in the concentrations of Au and As (Thomas et al., 2011). SIMS and LA-ICP-MS elemental maps revealed that Au is incorporated into pyrite as inclusions of free Au and Au in solid solution (Mumin et al., 1994; Large et al., 2009). Dissolution and

recrystallization of pyrite during various epigenetic ore-forming episodes, and mobilization of Au and As from the pyrite structure is well documented in the Sunrise Dam deposit, where inclusions of Au and arsenopyrite cluster along the corroded boundaries between different generations of pyrite (Sung et al., 2009).

Pyrite and arsenopyrite are the main hosts for "refractory" or "invisible" Au in orogenic gold deposits when precipitated under higher fS_2 conditions, and their role as an Au host becomes minor when Au-tellurides form. Gold mineralization is usually the result of sulfidation reactions between Au-bearing fluids and the Fe-rich wall rocks, and possibly pressure fluctuation. For Archean deposits, the temperatures of ore formation are variable between 325 and 400 ^{o}C, while temperature range is lower for, younger deposits (250-350 ^{o}C). Sulphur isotopic data show large variation in $\delta^{34}S$ values (-20 to +25), reflecting multiple sources for sulphur (Goldfarb et al., 2005; and references therein).

Pyrite is ubiquitous in porphyry Cu, and Cu-Au deposits, and forms over a wide range of temperatures in almost all types of alteration assemblages, including propylitic, sericitic, argillic, and potassic; preferentially pyrite concentrates in veins enveloped by sericite during medium temperature alteration (Seedorf et al., 2005). Depending on physico-chemical conditions, pyrite formation is coeval with the precipitation of chalcopyrite, molybdenite, magnetite, bornite, enargite, and tennantite. The size of euhedral and/or semi-euhedral grains of pyrite varies from few micrometers to 1 cm. Two types of textures are observed in pyrite from porphyry deposits: (i) pristine pyrite without detectable elemental zoning and with homogeneous distribution of trace elements; and (ii) grains of zoned pyrite with heterogeneous distribution of trace elements, which concentrate as solid solution or inclusions in fine-grained areas/overgrowths. Commonly As and Au partition into growth zones in pyrite that vary from submicrometer to few millimetres in thickness (Kouzmanov et al., 2010; Reich et al., 2013). However, relicts of sector zones are also preserved as reported

for pyrite from the Bingham and Rosia-Poieni porphyry deposits (Richards and Kerrich, 1993; Kouzmanov et al., 2010). Reich et al. (2013) reported comprehensive SIMS and EMPA analyses and elemental maps of trace elements in pyrite from the giant Dexing porphyry Cu deposit in China. The complex chemical zoning observed, coupled to the high Au-As-Cu abundances (~100-1000 ppm range) related to both solid solution and nanoparticulate incorporation. Studies of fluid inclusions show that metal deposition in porphyry copper deposits occurs in the field of coexisting brine and vapour. The low-salinity vapour (2-10 wt. % $NaCl_{equiv}$) is a major agent for metal transport in some porphyry systems, particularly for Au (Williams-Jones and Heinrich, 2005).

In epithermal Au deposits, pyrite contains up to percent levels of Au, As, and other trace metals (e.g., Richards and Kerrich, 1993; Deditius et al., 2009a). The trace elements concentrate in growth and/or sector zoning. The growth zones consist of colloform to fine-grained, nanoscale pyrite deposited on the "barren" euhedral to anhedral pyrite or it occurs as regular zones that reflect the euhedral morphology of the pyrite grains (Rosúa et al., 2003; Chouinard et al., 2005a; Deditius et al., 2008; Winderbaum et al., 2012). In numerous cases, growth and sector zoning alternated, and Au is present as both micro- to nano-particles and solid solution in As-rich pyrite (Pals et al., 2003). Nano- and micro-scale porosity associated with metallic nanoparticles in growth zones was reported from various epithermal deposits (Deditius et al., 2011a and b). The origin of this association was interpreted to be a result of far-from-equilibrium processes related to mixing of hydrothermal fluids of different compositions or dissolution-reprecipitation of pyrite under kinetically favoured conditions (Deditius et al., 2011a and b; Pačevski et al., 2012).

Pyrite in epithermal deposits formed under relatively low-temperature conditions 150-350 ^{o}C. In high-sulfidation systems, ore stage pyrite is associated with quartz, alunite, pyrophyllite, dickite, and kaolinite. In contrast, pyrite from low-sulfidation epithermal

deposits is associated with quartz, calcite, adularia, and illite. The stable isotope composition of ore and alteration minerals indicates that fluids of magmatic origin mixed with various proportions of meteoric water (Simmons et al., 2005; Williams-Jones and Heinrich, 2005).

Pyrite in volcanic-hosted massive sulfide (VHMS) deposits is characterized by extreme textural and size variability. Among most frequently reported textures are colloform, laminar, massive, granular, framboidal, dendritic, globular and anhedral-euhedral (McKibben and Elders 1985; Huston, et al., 1995; Barrie et al., 2009; Maslennikov et al., 2009). The size of individual pyrite grains ranges from few micrometers to few centimeters. Trace elements including Au and As mainly concentrate in growth zones. Most of the Au and As in pyrite in VHMS deposits occurs as solid solution at the concentrations below 50 ppm and 50,000 ppm, respectively. Gold and As in metamorphosed VHMS deposits and higher temperature parts of the volcanic chimneys of VHMS deposits were expelled from the pyrite structure and/or directly precipitated from the hydrothermal fluid, and form native Au, Au-tellurides, and various As-bearing minerals, and concentrations of Au may reach few hundred ppm (Huston, et al., 1995; Barrie et al., 2009; Maslennikov et al., 2009). The temperature of formation of pyrite in the VHMS deposits ranges from 420 ^{o}C to less than 100 ^{o}C, and depends on the position of the pyrite grain with respect to the central parts of the volcanic chimney; i.e., the closer the position of pyrite to the main conduit is the higher the temperature of its formation (Maslennikov et al., 2009).

Witwatersrand-type Au modified paleoplacer deposits host four generations of pyrite of detrital and post-sedimentary origin that have variable sizes from a few micrometer to a few centimeters. Broad classification of the textural types of pyrite includes round compact or porous pyrite, concentrically laminated pyrite, and compact pyrite of anhedral or euhedral morphology (Frimmel, 2005; Koglin et al., 2010; Agangi et al., 2013). Trace elements are distributed heterogeneously into growth zoning of several tens of micrometers thick, which is

a dominant type of zoning in pyrite from Witwatersrand deposit. Oscillatory, As-enriched growth zoning of pyrite is truncated in the grains that experienced mechanical abrasion (McLean and Fleet, 1989). BSE imaging, LA-ICP-MS elemental mapping, and single spot analyses revealed that the highest amount of Au (6.4 ppm on average) is hosted by round, porous or laminated pyrite, while < 1 ppm of Au characterizes compact detrital and anhedral/euhedral rims of post-sedimentary generations of pyrite. Arsenic tends to concentrate in the rims of the post-sedimentary pyrite. The post-sedimentary generation of pyrite hosts inclusions of free Au, as suggested by the Au-As relations in arsenian pyrite from the Witwatersrand deposit (Fig. 10E in Agangi et al., 2013).

The preservation of compositional zoning suggests limited mobilization of trace elements in the pyrite structure, including Au and As, during greenschist facies metamorphism of the sediments, which took place at temperatures of 350 ± 50 ^{o}C and pressure ≤ 3 kbar and interaction with hydrothermal fluids (Barnicoat et al., 1997; Philips and Law, 2000). Fluid inclusion studies document the presence of H_2O-rich fluids of moderate salinity (10-18 wt. % $NaCl_{equiv.}$), homogenization temperatures below ≤370 ^{o}C, and significant component of meteoric source for Au mobilization (Frimmel et al., 1999; Agangi et al., 2013; and references therein).

This summary confirms that pyrite is a widespread in a broad range of temperature settings, from sedimentary to magmatic hydrothermal (Craig et al., 1998). The increase in the temperature causes recrystallization and increase in the grain size of pyrite. In metamorphic terranes, pyrite is also subjected to the deformation, and local syn-kinematic growth, promoted by pressure solution that causes elongation of the pyrite crystals (Cook et al., 1993). Arsenic and Co zoning is preserved in pyrite up to temperatures of 500-600 ^{o}C and pressure of 6-9 kbar, as reported for pyrite from Sulitjelma deposit (Norway), and Grace Mine, Pennsylvania (US) (Craig et al., 1998). The Au growth zoning is also present in pyrite

from Bendigo (Australia), which experienced metamorphism at the temperature of ~350 ^{o}C (Large et al., 2009, and references therein). In the case of pyrite hosting nanoparticulate Au in metamorphosed deposits, it is expected that at least some Au will be hosted in the As-pyrite structure up to the temperature of 650 ^{o}C (Reich et al., 2006). During retrograde metamorphism, zoned pyrite grows at the expense of pyrrhotite, as the latter mineral is a common source of sulphur in numerous metamorphic terranes (Craig and Vokes, 1993).

Arsenic clearly facilitates the incorporation of Au in pyrite from all geologic settings, although the degree of incorporation appears to vary with temperature, chemical nature of the mineralizing fluids, and extent of fluid-pyrite interactions, porosity, and recrystallization processes.

3. SAMPLES AND METHODS

New pyrite EMPA and SIMS analyses presented here come from Carlin-type Au, low and high sulfidation epithermal Au, orogenic Au and porphyry Cu deposits (Tables 1-3). The investigated material represents a continuum of 20 years of research on numerous Carlin-type deposits (e.g., Arehart et al., 1993; Simon et al., 1999b; Reich et al., 2005; Deditius et al., 2011a). The pyrite samples from high-sulfidation deposits at Pueblo Viejo and Yanacocha constitute a significant part of drill-core profiles described in detail by Deditius et al. (2008) and Deditius et al. (2009). Three sets of samples from Butte porphyry Cu-Au deposit were kindly provided by Mark Reed. Owing to the relatively low concentration of trace elements pyrite mineral separates from orogenic Au deposits were investigated exclusively using SIMS, which allows a larger number of grains to be analysed for Au and As. Petrographic description of the analysed samples from Carlin-type and epithermal deposits can be found in Simon et al. (1999b), Reich et al. (2005), and Deditius et al. (2008, 2009a, b). In addition to the aforementioned sources, SIMS, EMPA, micro-PIXE and LA-ICP-MS data were compiled

from the literature for 60 different deposits (Table A.1).

The chemical composition of pyrite analysed for this study was determined by electron microprobe analysis (EMPA) using a Cameca SX100 at the University of Michigan Electron Microbeam Analysis Laboratory (EMAL). Elements and X-ray lines used for the analysis are Fe (K_α), S (K_α), As (L_α), Au (L_α), Pb (M_α), Se (L_α), Cd (L_α), Ag (L_α), Hg (M_α), Zn (K_α), Cu (K_α), Ni (K_α), Co (K_α), Sb (L_α), Te (L_α) and Si (K_α). Operating conditions included an accelerating voltage of 20 kV and beam current of 20-30 nA with wavelength-dispersive X-ray spectrometers (WDS). In order to improve the statistics of the count rates, counting times were 30 seconds for Fe, S and Si, 60 seconds for As, Cd, Pb, Zn, Cu, Ni and Co, 120 seconds for Se, Ag (140 seconds), Hg, Sb and Te, and 240/200 seconds for Au. The electron beam was focused to ~1 μm in diameter. Natural and synthetic standard specimens were used for calibration were FeS_2 (for Fe and S), FeAsS (for As), Sb_2S_3 (for Sb), HgS (for Hg), PbS (for Pb), CdS (for Cd), ZnS (for Zn), CuS (for Cu) SbTe (for Te), Au^0 (for Au), Ag^0 (for Ag), Ni^0 (for Ni), Co^0 (for Co), Se^0 (for Se) and $Fe_3Al_2(SiO_3)_4$ (for Si).

SIMS analyses were collected using Cameca IMS-3f ion microprobe (SIMS) at the Advanced Mineral Technology Laboratory (AMTEL), London, Ontario. The analyses were conducted with a Cs^+ primary beam at a current of 10-15 nA producing an analytical spot size of approximately 20 micrometers diameter and 1-3 μm depth. Secondary ions monitored include ^{32}S, ^{56}Fe, ^{63}Cu, ^{65}Cu, ^{75}As, ^{80}Se, ^{109}Ag, ^{123}Sb, ^{130}Te and ^{197}Au. Molecular interferences for Au(1) were eliminated by 180 V offset. Minimum detection limits (2σ) in parts per million were 1 for Cu, 2 for As, 0.2 for Se, 6 for Ag and Sb, 0.2 for Te, and 0.3 for Au. Elemental scans were carried out at different speeds depending on the element analysed, with detection limits that were usually 2 to 5 times higher than for spot analyses.

4. RESULTS

4.1 Chemical composition of pyrite

New EMPA analyses of pyrite are given in Table 1, and new SIMS analyses of pyrite from Carlin-type deposits are presented in Table 2. Table 3 summarizes new SIMS analyses of Au and As in pyrite from orogenic Au deposits (Kanowna Belle, Golden Pond), and from the Ok Tedi porphyry Cu-Au deposit. SIMS analyses from the Lancefield, Mickey Doolan, New Celebration and Sons of Gwalia orogenic Au deposits published by Vaughan and Kyin (2004) are also shown in Table 3 for comparison.

Zoned pyrite from Carlin-type deposits has the highest As concentrations from all studied deposits, i.e., 18.6 wt. % for Betze Post and 7.7 wt. % for Twin Creeks. Also, highest concentrations of Au (0.19 wt. %) were measured in pyrite from the Lone Tree Carlin-type deposit (Table 1). Antimony, Cu and Te are also commonly reported in the As-rich zones in pyrite from this type of deposits (Barker et al., 2009). Fine-grained, collomorphic pyrite from the Yanacocha high-sulfidation epithermal Au deposit has variable trace element concentrations (Table 1), including As concentrations up to 5.52 wt. %. In general, the As content of these pyrites increases with decreasing grain size (Deditius et al., 2008). High Au contents were measured in pyrite from samples CHQ-606 N3 and CHQ-470 N4 (Yanacocha), with maximum amounts of Au at 0.46 wt. % and 0.11 wt. %, respectively (Table 1). Pyrite from the Pueblo Viejo high-sulfidation epithermal Au deposit in the Dominican Republic show moderate concentrations of As (≤ 3.41 wt. %) (Deditius et al., 2009a). These pyrites contain higher amounts of Ag (≤ 1.41 wt. %), than Au (≤ 0.16 wt. %), respectively. Unlike pyrites from Carlin-type and epithermal Au deposits, euhedral, semi-euhedral and pristine pyrites from the Butte porphyry Cu deposit in Montana contain low concentrations of trace

elements. Arsenic contents are < 600 ppm and Au was not detected during EMPA analysis (Table 1).

The lower detection limits of SIMS analyses presented in Tables 2 and 3 allowed: (i) recognition of larger variations in the amount of As and Au for high-Au-As samples, and (ii) clarification of Au-As relations in samples containing trace element concentrations below the detection limits of EMPA. In pyrite from Carlin-type deposits, As concentrations vary significantly from a minimum of 36 ppm in Deep Star to a maximum of 18.6 wt. % in Betze Post (Table 2). Highest concentrations of Au, 2520 ppm, were detected in pyrite from the Meikle deposit. In orogenic Au deposits, maximum contents of Au and As are 92 ppm and 2.64 wt. %, respectively (Kanowna Belle). The smallest contents of Au and As, which are in the New Celebration deposit, are 0.03 ppm and 0.47 ppm, respectively (Table 3). In the Ok Tedi porphyry Cu-Au system, concentrations of Au and As in pyrite vary from 0.21 to 16.6 ppm, and from 2 to 3800 ppm, respectively (Table 3). The detailed discussion of the relationships between As and Au is provided below.

4.2 Relationships between Au and As in pyrite

EMPA analyses reveal an antithetic relation between As and S and no relation between As and Fe in samples from Carlin-type deposits and one sample from the Yanacocha high-sulfidation epithermal deposit; YS-734 N2 (Fig. 3a and b). These relations indicate substitution of As for S in the pyrite structure, as suggested by Fleet and Mumin, (1997) and Reich et al. (2005). Other analysed samples from Yanacocha reveal an antithetic relation between As and Fe, that reflects substitution of As for Fe. The Yanacocha pyrites (except YS-734 N2) also show a positive relation between As and Au, and Pb and Se (Deditius et al., 2008). Arsenic-sulphur relations for pyrite from Pueblo Viejo plot between trends for Carlin

and Yanacocha (Fig. 3a and b) As vs. Fe relations for pyrite from Pueblo Viejo follow the trend seen for Carlin deposits. Deditius et al. (2009b) showed that As-S relations for Pueblo Viejo reflect the presence of nanoscale inclusions of amorphous As-Fe-S that contain up to 10 at. %, (18 wt. %) of As. SIMS analyses also show positive relations between Au and Ag and Sb, as well as between Te and Au, Ag and Sb (Fig. 3 c and d).

The relation between Au and As in pyrite from Carlin-type Au, epithermal Au, porphyry Cu and Cu-Au, and orogenic Au deposits is shown in Figures 4a-c. Most of the analytical data points for pyrite in Carlin-type deposits cluster into a broad area showing a positive relation between Au and As (group 1, Fig. 4a). A few analytical points, probably representing analyses contaminated by inclusions of native Au, deviate from group 1 (group 2, Fig. 4a). The upper limit of this characteristic wedge-shaped zone was interpreted previously by Reich et al. (2005) as the solubility limit of Au as a function of As in pyrite (Fig. 4a). In contrast, the data from orogenic Au deposit form only one cluster of points, similar to the "wedge-shaped" zone of Carlin-type pyrites, and no data points occur above the well-defined wedge-shaped zone (Fig. 4b). It is important to note that the amounts of Au and As in pyrites from Carlin and epithermal Au deposits are generally one to two orders of magnitude higher than those in pyrites from orogenic Au and porphyry Cu deposits (Fig. 4c). Pyrite analyses from epithermal Au deposits show the highest Au:As ratios and plot above the 1:100 line while analyses of pyrite from Carlin-type and orogenic Au plot below this value with a few outliners (Fig. 4c). In contrast, analyses of samples from porphyry Cu deposits (e.g., Ok Tedi) plot between the 1:100 and 1:10 lines (Fig. 4). Data also show that, in general, pyrite from porphyry Cu and orogenic Au deposits are depleted in As when compared with pyrite from Carlin-type and epithermal Au deposits, with most analyses plotting below the 10,000 ppm (or 1 wt. %) limit of As (Fig. 4c).

5. DISCUSSION

Most of the discussion will refer to Carlin-type Au, orogenic Au, porphyry Cu and Cu-Au, and epithermal Au deposits. Existing Au-As data of pyrite from VHMS, IOCG, Witwatersrand Au, and coal deposits, although limited, allow some conclusions about the behaviour of As and Au in hydrothermal systems.

The observations summarized above suggest that pyrites from different types of hydrothermal ore deposits are characterized by different ranges of Au-As concentrations. In the next section, we develop this idea by combining Au-As analytical results in pyrite with previously published Au-As compositions measured in natural and synthetic fluid inclusions. Our aim is to couple mineral and fluid chemistry, and to explore the use of pyrite as a geochemical tracer for Au and As in hydrothermal ore deposits.

5.1 Carlin-type deposits

Pyrite analyses from Carlin-type deposits form a wedge-shaped zone with most analyses plotting below an Au:As ratio of 1:100 (Fig. 5a). Reich et al. (2005) reviewed XANES and EXAFS data showing that both Au^{+} and Au^{0} were present in fine-grained, porous pyrite as shown in Figure 5a. The distribution of Au-As pyrite analyses below the solubility limit suggests that Au-bearing fluids in Carlin systems were undersaturated with respect to native Au during precipitation of As-pyrite, as previously suggested by Reich et al. (2005) (Fig. 5a). There are no available quantitative LA-ICP-MS data of Au-As in fluid inclusions (quartz or other minerals) from Carlin-type deposits in Nevada. This is due to the small size of the fluid inclusions (< 2 μm) and the difficulty to elucidate their paragenetic relationships with associated minerals (Hofstra and Cline, 2000). In contrast, fluid inclusions in quartz from the

Chinese Shuiyindong and Yata Carlin-style are larger, (~20 μm), and of aqueous-carbonic and carbonic composition (Su et al., 2009). It is noteworthy to mention that visible gold is reported at Shuiyindong deposit (Su et al., 2009). The textures of fine-grained arsenian pyrite deposited on pre-ore coarser pyrite in the Chinese Carlin-style deposits and classic Carlin-type deposits from Nevada are very similar. Therefore, the available Au-As LA-ICP-MS data in fluid inclusions from the Chinese Carlin-style deposits (e.g., Su et al., 2012) are included in the following discussion, keeping into consideration the differences between both styles of mineralization (Chinese vs. Nevada Carlin ores).

These analyses of fluid inclusions from Chinese deposits reveal that the content of Au and As in the mineralizing fluid was relatively high, ≤7.8 ppm and ≤340 ppm, respectively. The Au:As ratio of this fluid was ~1:100 (Fig. 5b), similar to the Au:As ratios measured in the ore-stage pyrite (Su et al. 2012; Fig. 5 therein) (Fig. 5b). Pyrite from the aforementioned deposits contains two forms of Au (nanoparticulate and solid solution) and plot near the solubility limit in Figure 5a. Consequently, it is likely that the Au:As ratio of 1:100 represents the approximate saturation state of the ore fluid with respect to native gold during the formation of arsenian pyrite. Therefore, massive precipitation of arsenian pyrite may result in about one order of magnitude depletion in Au content in the ore fluid (Fig. 5b). No significant changes were noticed in As concentration in fluid inclusions through the paragenesis in spite of precipitation of arsenopyrite at the latest stage of As-pyrite formation (Su et al., 2012).

These observations confirm the high capacity of arsenian pyrite to incorporate Au from hydrothermal fluids. However, the fine-grained, porous and irregular nature of arsenian pyrite textures in Carlin-type deposits (Palenik et al., 2004) suggests that efficient scavenging of Au from solution is dominated by the kinetics of pyrite precipitation rather than high-T equilibrium partitioning, as discussed below. The general "undersaturated" nature of Carlin-

type fluids, coupled with the high pyrite surface area would enhance chemisorption and substitution as the dominant mechanisms of Au incorporation into pyrite in these systems. The process of chemisorption was advocated by Muntean et al. (2011 and references therein) who supported formation of Au-bearing As-pyrite in Carlin-type deposits via chemisorption of Au, transported as $Au(HS)_2^{1-}$ and $AuHS^0$ species, on the Fe-depleted surface of pre-existing As-pyrite at temperatures between ~180 and 240 ^oC.

The negative correlation between As and S in pyrite from Carlin-type deposits (Fig. 2) suggests a mechanism of Au-incorporation such as that shown by Reaction 1:

$$Fe(S,As)_2 + 2Au(HS)^0 \quad Fe(S,As)_2\text{-}Au_2S + H_2S \quad \text{Reaction (1)}$$

where As substitutes for S (Simon et al., 1999b). This reaction does not incorporate the effect of Fe-vacancies, i.e., the role of Fe-depleted, mineral surface. This is also important in the context of the high-resolution transmission electron microscopy (HRTEM) observations of the Au-rich rims of arsenian pyrite, which showed that Au was deposited during growth of micro- to nanoparticulate As-rich rims of pyrite, not on the surface of pre-existing euhedral pyrite (Palenik et al., 2004). This suggests a mechanism characterized by simultaneous precipitation of pyrite and incorporation of Au. In order to assess the effect of Fe-depleted surfaces, we have analysed a well-studied case of pyrite from Deep Star Carlin-type deposit where all Au is in solid solution (sample DS-03-04 in Reich et al., 2005). Reaction 2 shows the formation of one mole of Fe-depleted arsenian pyrite hosting Au in solid solution from main and trace cationic components, and H_2S (Fig. 5a):

$$0.9Fe^{2+} + 0.006Ni^{2+} + 0.004Hg(HS)_2 + 0.001Au(HS)^0 + 1.791H_2S + 0.19As(OH)_3 + 0.002Sb(OH)_3 \quad (Fe_{0.9}Ni_{0.006}Hg_{0.004}Au_{0.001})_{0.911}(S_{1.8}As_{0.19}Sb_{0.002})_{1.992} + 0.576H_2O + 0.6H_2 + 1.812H^+.$$

Reaction (2)

The amount of missing charge/vacancy (~ 0.09) in the cationic position is only partly

balanced by incorporated metals in Reaction 2. Consequently, it is unlikely that such a significantly unbalanced charge (close to 10 %) could be accommodated by euhedral grains of pyrite, supporting the notion that surface kinetics are more effective in incorporation of Au in arsenian pyrite. The formation of Fe-deficient arsenian pyrite would then require a source of Fe^{2+}, which may be satisfied by partial dissolution of pre-existing (diagenetic) pyrite, and formation of local reducing conditions that would promote destabilization of Au-S complexes and subsequent Au-deposition (Pokrovski et al., 2002b), or an external source of Fe from dissolution of carbonates (Hofstra and Cline, 2000). Thus, the proposed mechanism is consistent not only with geological evidence but also with the previously reported mineralogical features of Carlin pyrite, e.g., cationic deficiencies, abundant trace metal contents (and variety), and nonsystematic distribution of Au (Johan et al., 1987; Fleet and Mumin, 1997; Hofstra and Cline, 2000).

5.2 Orogenic Au deposits

Gold-arsenic relations of pyrite in orogenic Au deposits also show a well-defined wedge-shaped zone in log-log compositional space. Figure 6a shows that As in pyrite from orogenic deposits controls the behaviour of Au in a way similar to that in Carlin-type systems (with the exception of the Dongping analyses, which form a vertical trend (Fig. 6a). In orogenic deposits, the analysed pyrite is related to a large variety of protholith including: black shales, intermediate volcanic rocks, granitic rocks and felsic porphyries, banded iron formations; and host-rocks include: dolerite, basalts, metabasalts, syenite, and ryodacite (Ho et al., 1995; Large et al., 2007; Wood and Large 2007; Morey et al., 2008; Cook et al., 2009; Sung et al., 2009; Thomas et al., 2011; Valásquez et al., 2014). Most pyrite analyses in these systems cluster within the same area in Au-As plots. Therefore, no further sub-divisions beyond the

classification of "orogenic gold deposits" were implemented. Pyrite in orogenic deposits usually contains less than 100 ppm Au. Higher Au concentrations are mostly due to the presence of Au nanoparticles (Vaughan and Kyin, 2004), such as the analyses of Sung et al. (2009) and Cook et al. (2009) showing Au concentrations of ~3000 ppm and 11,500 ppm, respectively, both of which are due to inclusions of Au-bearing minerals (Ciobanu et al., 2012).

The upper limit of the wedge-shape zone (1) in orogenic gold deposits is defined by an Au:As ratio of about 1:10, although the analyses are distributed heterogeneously (Fig. 6a). Approximately 75 % of the analyses cluster into a smaller wedge-shape zone (2), with an upper limit at an Au:As ratio of about 1:400 (Fig. 6a). While the wedge-shape zone (1) breaches the solubility limit of Au for Carlin-type deposits (red line in Figure 6a), the wedge-shape zone (2) plots entirely below the solubility limit. This suggests that Au-As relations in orogenic deposits may be controlled by a different solubility limit than Carlin deposits (Fig. 6a). These differences are most likely a reflection of a more complex evolution of pyrite in orogenic Au deposits, where up to 6 generations of pyrite are reported. In these systems, Au-bearing, coarse pyrite precipitated from hydrothermal fluids , and its trace-elements composition was modified under high-temperature conditions (300-400 ^{o}C), with at least partial re-equilibration with Au-bearing fluids (e.g., Mumin et al. 1994; McClenaghan et al., 2004; Morey et al. 2008; Sung et al., 2009). In the distal parts of orogenic Au deposits framboid relics are observed suggesting that pyrite grew at the expense of an earlier, fine-grained seed under fluid-assisted conditions (Large et al., 2007; and Large et al., 2009). Therefore, pyrite from orogenic systems commonly undergoes Au remobilization leading to Au enrichment in the altered areas (Morey et al., 2008), a process that increases Au concentrations by two orders of magnitude compared with homogeneous primary pyrite. Figure 6b displays the impact of Au remobilization on Au-As concentrations in pyrite from

the Golden Ridge deposit, described by Morey et al. (2008), upon alteration and/or deposition of Au by a hydrothermal fluid. This process usually leads to gold enrichment with no significant change in As concentration, and Au occurs as native Au nanoparticles (blue circles Fig. 6b). In contrast, samples reported by Sung et al. (2009) at Sunrise Dam deposit contain both solid solution and nanoparticulate Au (black arrows pointing to green circles), both of which plot below the solubility limit (Fig. 6b). This apparent deviation from the predicted behaviour was interpreted by Sung et al. (2009) and Cook et al. (2009) to be caused by extensive recrystallization of pyrite that resulted in liberation of Au from the pyrite structure, Au migration, and subsequent formation of Au nanoparticles. In addition, during higher temperature stages of mineralization the Au-bearing nanoparticles may dissolve back into the structure of pyrite as suggested by Cook et al. (2009) who performed heating experiments on natural pyrite from Dongping at temperatures of 330 ^{o}C and 420 ^{o}C. The analyses of pyrite compositions from these experiments plot close to or below the solubility limit of Au (Fig. 6b). Accordingly, the lower contents of Au in arsenian pyrite from orogenic Au deposits are a due to consequence of the higher temperature of their formation than pyrite from Carlin-type and epithermal deposits, complex fluid-induced, recrystallization histories of pyrite and subsequent Au mobilization (e.g., Large et al., 2007; Morey et al., 2008).

Based on the distribution of Au-As data points and the occurrence of nanoparticulate vs. solid solution Au, we propose that the solubility limit of Au in arsenian pyrite in orogenic deposits approximates the line: $C_{Au} = 0.004 \cdot C_{As} + 2 \cdot 10^{-7}$, which is two orders of magnitude lower than the solubility limit for Au in the Carlin-type deposits (Fig. 6c). The differences in the distribution of the analytical data between Carlin-type (Fig. 5) and orogenic deposits (Fig. 6) in Au-As space probably reflect the different conditions and thus processes that were responsible for the formation of Au-bearing NPs in pyrite, and evolution of pyrite composition under changing physico-chemical conditions. In Carlin-type deposits, Au

chemisorbed to As-rich mineral surfaces led to the formation of metastable (Au,As)-rich pyrite, and Au was subsequently exsolved as Au NPs and/or associated As-minerals. In orogenic Au deposits at least part of the pyrite grains were affected by dissolution and/or reprecipitation upon interaction with hydrothermal fluids delivering Au, and causing chemical redistribution of the data in Au-As space (Fig. 6b). In addition, the differences in the Au-As composition between the pyrite from Carlin-type and orogenic Au deposits may be related to the re-equilibration of pyrite compositions during protracted cooling and/or heating processes in the latter ones.

Additional differences in the Au-As distributions of data may be due to Au and/or As remobilization from the pyrite structure during mineral/fluid interaction, which resulted in the formation of nanoscale porosity as an effect of dissolution-reprecipitation reactions (Putnis, 2009, and references therein). These textural features are observed in pyrite from all types of ore deposits. The porous arsenian pyrite from Carlin-type deposits contains warm-like channels that consist of polycrystalline pyrite. The association of these channels with Au and Ag-Pb-S NPs suggest that they may facilitate migration of the altering fluid that enhances metal mobilization during the dissolution processes (Deditius et al., 2011a). In arsenian pyrite from Sunrise Dam, intense dissolution-reprecipitation processes are responsible for Au and As mobilization and formation of particulate Au and arsenopyrite (Sung et al., 2009). On the other hand, in the As-free pyrite from Dongping, China, porosity was a pathway for migration of highly volatile, Te-enriched hydrothermal fluid that deposited nanoparticulate Au-tellurides. Porosity was also developed in the Au-Te NPs (Ciobanu et al., 2011; Ciobanu et al., 2012). Nanoscale porosity in pyrite from epithermal ore deposits is tightly related with the formation of trace-element rich growth zoning. Randomly oriented nanopores were found in the Sb-rich growth zones in pyrite from Lone Tree deposit. These pores were surrounded by Fe-As-Sb-Pb-Ni-Au-S and Au-Ag-As-Ni-S NPs, which suggests direct precipitation from

a fluid rather than exsolution from the pyrite structure (Deditius et al., 2011a). A similar interpretation was proposed for the porous, polycrystalline Cu-rich zones observed in pyrite from Pueblo Viejo deposit, where authors suggested rapid kinetically-controlled deposition of Cu-Fe-S NPs plus porosity development, probably during boiling of the hydrothermal fluid (Deditius et al., 2011a and b). Porosity was also observed in the zones of microparticulate chalcopyrite deposited on the surface of Cu-rich pyrite at the Dexing porphyry Cu-Au deposit. This association was interpreted to be a result of the supersaturation of hydrothermal fluid with respect to chalcopyrite (Reich et al., 2013). Consequently, porosity in pyrite may act as an intra-mineral conduit for the hydrothermal mineralizing fluid that enhances metal remobilization from the pyrite structure or from the (Au,As)-bearing NPs.

5.3 Porphyry and epithermal deposits

Unlike Carlin-type and orogenic Au deposits, trace element data in pyrite from porphyry Cu deposits are very limited (Pass, 2010; Reich et al., 2013; and this paper). Gold in pyrite from porphyry Cu deposits seems to be distributed relatively homogeneously with no detectable zoning. However, it forms metal nanoparticles together with other metals and sulfides when the dominant metal can no longer be hosted as solid solution in the pyrite structure. Recently, Reich et al. (2013) documented the occurrence of Au nanoparticles and solid solution Au in samples from the quartz-sericite alteration stages at Dexing. Here, Au is in solid solution and also forms Au nanoparticles, and As-S correlations indicate that As occurs as As^{1-}. When these data are complemented with our analyses from the Ok Tedi deposit (Table 3), most points form a cluster with Au:As ratios from 1:1 to 1:10,000; with a few outliners (seven analyses with 500-700 ppm Au and ≤2.6 wt. % of As probably reflect the presence of Au NPs) (Fig. 7a). Gold-arsenic relations in Figure 7a suggest that

hydrothermal fluids in porphyry systems are undersaturated with respect to native Au, and Au and As are most likely incorporated into pyrite and other sulphide minerals under equilibrium conditions (400-600 ^{o}C) with only minor re-equilibration. Despite the lack of spectroscopic analyses, chemisorption of Au from ore fluids onto As-rich, early pyrite generations (Fleet and Mumin, 1997) or dissolution and precipitation of porous Au nanoparticles on reduced surface of As-pyrite (Pokrovski et al., 2002a; Deditius et al., 2008; Deditius et al., 2011a and b) may also be mechanisms of Au uptake in porphyry Cu deposits, especially in low-temperature veins and transitional (epithermal) stages of mineralization.

Analyses of pyrite from epithermal Au deposits form two clusters of data points that range in Au:As ratio from 1:1 to 1:10,000 (Fig. 7b), similar to ranges defined for porphyry Cu deposits (Fig. 7a). Concentrations of Au and As in epithermal deposits are higher than porphyry systems, as expected (Fig. 7b and c), and some Au and As analyses fall above the Au solubility limit defined by Reich et al. (2005). Most of the trace elements in pyrite in epithermal Au deposits are located in growth and sector zones, often in alternating zones that are indicative of surface (kinetic) or crystal-chemically (equilibrium) growth during metal deposition, respectively (Chouinard et al., 2005a; Deditius et al., 2009a).

Gold-arsenic clusters of points of porphyry and epithermal deposits overlap significantly (at Au 0.19-16.6 ppm and As 20-3765 ppm (Fig. 7c)). This suggests similar proportions of Au and As in the mineralizing fluid and/or similar conditions/mechanisms of Au and As incorporation into pyrite. However, a substantial fraction (~30 %) of Au-As analyses from epithermal deposits plot above the solubility limit for Au (Fig. 7b), confirming the dominant state of Au supersaturation for mineralizing fluids in these systems. The analyses plotting above the solubility limit may also indicate the presence of trace-element-rich pyrite nanoparticles. Indeed, the 8-900 nm nanocrystalline pyrite reported at the Yanacocha high-sulfidation Au deposit contains ≤450 ppm of Au and ≤5 wt. % of As as solid solution, but data

points plot above the solubility limit of Au (Fig. 7b). Despite this fact, a large proportion of pyrite analyses (~70 %) plots below the solubility limit reflecting the capacity of pyrite to scavenge Au from solutions undersaturated with respect to native Au. For example, the highest concentrations of Au in solid solution, 2952 ppm, was reported for pyrite from the Emperor deposit (Pals et al., 2003) (Fig. 7b).

The higher concentrations of Au in pyrite noted for some of the high-sulfidation epithermal Au deposits may also reflect their relatively oxidizing conditions of formation when compared with low-sulfidation systems, which could favour formation of Au^{3+} and $As^{2+,3+}$ species might be present in the pyrite structure (Chouinard et al., 2005a and b; Simmons et al., 2005; Deditius et al., 2008). Cationic As might stabilize or favour growth of pyrite nanoparticles due to structural misfit, leading to a higher capacity for incorporation of Au. Deditius et al. (2008) showed that pyrite containing cationic As incorporates higher amounts of Au than As-pyrite hosting anionic As (at the same amounts of As). Such an inverse relationship between the amount of incorporated Au and the size of As-pyrite crystals was observed in pyrite that hosts anionic (Simon et al., 1999b) and cationic (Deditius et al., 2008) species of As.

The position of Au-As data points relative to the solubility limit in Figure 7c indicates that saturation of Au in pyrite from porphyry and epithermal deposits is similar to the limit for Au in As-pyrite from the Carlin-type deposits $C_{Au} = 0.02 \cdot C_{As} + 4 \times 10^{-5}$ (Reich et al., 2005). However, the analyses of pyrite from porphyry Cu and epithermal Au deposits do not form a wedge shape-zone similar to that reported for Carlin-type pyrite (Fig. 6a). Instead, they form a positive trend along an Au:As ratio of 1:100 (Fig. 7c). The lack of a wedge-shape zone for Au and As analyses might be related to differences in the composition of the mineralizing fluid or conditions of pyrite formation. Pyrite in Carlin-type deposits form under low-temperature (< 240 ºC) conditions due to sulfidation of wall-rock and forms disseminated

aggregates (Hofstra and Cline, 2000; Muntean et al., 2011), while pyrite in porphyry-epithermal deposits forms at somewhat higher-temperatures from fluids that undergo boiling, cooling, and fluid mixing (Seedorf et al., 2005; Simmons et al., 2005).

5.4 Additional insights into pyrite geochemistry from other types of ore deposits

Additional insights into the behavior of Au and As in pyrite as a function of temperature can be gained from published data from VHMS, active hydrothermal vents in submarine environments, Witwatersrand Au, IOCG and coal deposits (Fig. 8). On the high-temperature side, ores from metamorphosed VHMS deposits shed light on the behavior of auriferous arsenian pyrite under metamorphic conditions. McClenaghan et al. (2004) suggested that substitution of As into primary pyrite as $[AsS]^{3-}$ and/or As_2 species promoted incorporation of trivalent cationic Au and Sb in the metamorphosed VHMS deposit at Bathrust in Canada. The authors noted that during metamorphism and mobilization of solid solution Au (that subsequently formed Au nanoparticles), the Au-rich inclusions clustered around As-rich domains of pyrite and mobilization of Au did not appear to reflect the changes in temperature or metamorphic grade. The analyses for pyrite with Au nanoparticles from Bathrust (yellow circles in Figure 6b, and black dashed circles in Figure 8) plot below the solubility limit of Au and within the same range of Au and As concentrations as the analyses of As-pyrite with Au nanoparticles reported at Sunrise Dam by Sung et al. (2009). The coexistence of nanoparticulate and solid solution Au in one deposit, commonly in one grain of pyrite, might reflect re-aggregation or assimilation of Au nanoparticles by diffusional exchange between the particles and the sulphide matrix. This Ostwald ripening-type process is best envisaged by the in-situ HRTEM experimental data by Reich et al. (2006), who documented coarsening of larger Au nanoparticles (>10 nm) in arsenian pyrite at the expense of the smaller ones (<4

nm), at temperatures of up to 650°C, with no visible changes in the As behaviour at the nanoscale. This process increases Au concentrations in pyrite, leaving the As contents more or less unchanged. Therefore, temperature-driven coarsening of Au nanoparticles might explain the presence of colloid-sized Au nanoparticles in As-poor or As-rich zones (Mumin et al., 1994; Huston et al., 1995), where Au/As analyses display vertical patterns in Au-As compositional space (e.g., Figs. 6a and b); although Au nanoparticle formation in pyrite from a secondary hydrothermal fluid cannot be discounted (Large et al., 2007; Morey et al., 2008).

The content of Au in pyrite from submarine hydrothermal vents, which are modern analogues of the VMS deposits, tends to increase with increasing distance from the central part of the hydrothermal chimney, a relation that has been interpreted to reflect a decrease in the temperature gradient from ~450 °C down to ~80 °C (Maslennikov et al., 2009). This gradient is reflected in Au:As ratios that change from <1:10,000 for pyrite from the high-temperature parts of chimneys down to 1:100 by the low temperature pyrite (Fig. 8). This change in the ratios supports the notion discussed above that changes in Au concentrations in pyrite are more sensitive to temperature than changes in As.

On the lower temperature side, pyrite from the Witwatersrand paleoplacer deposits provides additional insights about Au speciation. The sedimentary origin and complex evolution of pyrites from Witwatersrand (Frimmel et al., 2005; Law and Phillips, 2005; Agangi et al. 2013; and references therein) is indicated by the large variation in Au:As ratio crossing the solubility limit; from <1:10,000 up to >1:10 (Fig. 8). Such a wide range of ratios suggests the presence of Au in both solid solution and nanoparticulate settings. Indeed, LA-ICP-MS time-resolved depth profiles of pyrite revealed the presence of Au NPs in porous, trace element rich detrital pyrite, and vein-stage, recrystallized pyrite that formed during the peak of metamorphism (Agangi et al., 2013). These analyses plot next to (above and below) the solubility limit of Au in arsenian pyrite from Carlin-type deposits (Fig. 8). Consequently,

it is suggested that Witwatersrand pyrite exhibits a coupled Au-As geochemistry similar to that of Carlin-type and orogenic deposits.

One of the highest concentrations of Au, ≤3700 ppm, is reported for As-pyrite (≤5.76 wt. % of As) from a coal deposit in Xingren County (China), which was affected by hydrothermal fluids migrating along structural discontinuities (Ding et al., 2001; and references therein). The crystal-chemistry of Au and As in this pyrite has not been addressed, but the position of data points above the solubility limit suggests Au accumulation as nanoparticles or accumulation of Au in solid solution in nanoparticulate As-pyrite (Fig. 8). Finally, the lowest concentrations of Au (< 0.4 ppm) coupled to the highest concentrations of As (13.6 wt. %) in pyrite occurs in the Ernest Henry IOCG deposit (Fig. 8) (Foster et al., 2007). The low amount of Au in pyrite in this locality is probably due to the high-temperature of mineralization, ~450 ^{o}C, and deposition of Au in the native form.

5.5 Retrograde solid solubility of Au and As in arsenian pyrite

Gold-arsenic relations not only help constrain the chemical limits of these two elements in pyrites from various types of ore deposits, but also provide key information on the approximate temperature controls on Au incorporation into arsenian pyrite. A review of formation temperatures of natural and synthetic auriferous arsenian pyrite (Table A.1) suggests that both Au and As have retrograde solid solubility behaviour, a feature that has been previously recognized in P-doped semi-conductors (O'Shaughnessy et al., 1974). Figure 9a shows that Au anti-correlates with temperature of formation estimated for host deposits (r^2 = 0.5), a feature that confirms observations suggesting Au remobilization from the pyrite structure at higher temperatures up on recrystallization of fine grained pyrite of framboidal, sooty or colloform morphologies into euhedral crystals and formation of Au-bearing metallic

particles (Huston et al., 1995; Goldfarb et al., 2005; Large et al., 2009; Maslennikov et al., 2009; Thomas et al., 2011). The experimental studies on Au partitioning between pyrrhotite, pyrite, magnetite, and chalcopyrite confirm low contents of Au, about 2 to 6 ppm, in pyrite at 600 ^{o}C and 700 ^{o}C, respectively (Cygan and Candela, 1995). Under lower temperature conditions of 500 ^{o}C, the amount of Au in pyrite remains at a similar level of a few ppm, when the As concentration is ≤ 180 ppm (Tausson, 1999). Our analyses show that the solid solution content of Au in pyrite changes from ~300 ppm at 200 ^{o}C, down to ~0.1 ppm, at 500 ^{o}C, following the exponential relation:

$$C_{Au} = 0.0187 \cdot e^{-0.0234T}$$

Equation (1)

where, C_{Au} stands for Au concentration in ppm and T is temperature (^{o}C). Despite the relatively large error (Fig. 9a) this general relation shows that the concentration of Au in pyrite should be ≤ 33 ppm at the temperature > 300 ^{o}C. This value agrees relatively well with the content of Au in pyrite in orogenic deposits (Wood and Large, 2007; Sung et al., 2009). At lower temperatures (~100 ^{o}C) the content of Au reaches unrealistic values of 3500 ppm. However, high concentrations are often reported in arsenian pyrite formed at low temperatures and that contain nanoparticulate Au instead of solid solution Au (Figs. 5-8).

In Figure 9b the effect of temperature on the As content in pyrite is explored. The plot of As *vs*. temperature also shows a negative correlation with temperature (r^2 = 0.36). However, the value of the correlation coefficient is lower due to the nine pyrite analyses from As-depleted environments (Table A.1). If these analyses are not included then the r^2= 0.47, and the best-fit curve is**:**

$$C_{As} = 0.4785 \cdot e^{-0.0143T}$$

Equation 2

Based on this equation, calculated concentrations of As decrease from ~20,000 ppm at

200 °C to ~250 ppm at 500 °C (Fig. 9b). These As values are commonly reported for pyrite from Carlin-type, epithermal, orogenic and porphyry deposits (e.g., Emsbo et al., 2003; Pals et al., 2003; Reich et al., 2005; Large et al., 2007; Barker et al., 2009; Deditius et al., 2009a; Sung et al., 2009; Pass, 2010; Reich et al., 2013; Velásquez et al., 2014).

From these relations we suggest that Au has retrograde solubility in pyrite as a function of As content and temperature, and that it behaves in a manner similar to phosphorous impurities in silicon semiconductors (O'Shaughnessy et al., 1974). This decreasing As concentration in pyrite with increasing temperature in combination with the presented solubility limits suggests that the behaviour of Au in pyrite may be strongly related to the position of As atoms with respect to interstitial Au. So far there is no evidence that As coordinates Au atoms in the pyrite structure. Simon et al. (1999a) reported that Au forms 2- or 4-coordinated units with S atoms, not with As^{1-}.

Additional clues about inverse relations between Au+As and temperature can be drawn based on research of Au electrodes. For example, Tokhomirova et al. (1994) reported formation of Au_xAs_y intermetallic compounds (x = 1-3; y = 2-6) on the surface of the Au electrode. Consequently, we revisit the common paradigm that assumes As-rich Fe-depleted surface of pyrite as the attractive platform for Au deposition (Fleet and Mumin, 1997), and propose that in some cases it may be the Au atoms in the pyrite structure that attract As. Examples can be found in porphyry, high-sulfidation epithermal, and Carlin-type deposits where at least part of As and Au were deposited contemporaneously in pyrite (Barker et al., 2009; Deditius et al., 2008; Deditius et al. 2009a; Reich et al., 2013), and in some cases formed As-Au-bearing metallic NPs (Deditius et al., 2011). In addition, it was reported that as little as three monolayers of As limits the growth of the Au NPs (Dinan et al., 1989). By analogy the As-rich nanozones in pyrite may be responsible for the relatively uniform size of Au NPs in Carlin-type and epithermal deposits; i.e., < 50 nm (Reich et al., 2006; Deditius et

al., 2011). These As-rich nanozones are likely to recrystallize under higher temperature conditions facilitating Au diffusion and migration.

The decrease in As concentration in pyrite with increasing temperature may be related to the removal of defects and growth of As-rich domains in the pyrite structure under equilibrium conditions, promoted by relatively slowing cooling rates and/or protracted heating events. Thus, a decrease in distortion may enhance the accommodation of large Au ions into the interstitial positions (Fleet and Mumin, 1997; Simon et al., 1999a). On the other hand, precipitation of As-pyrite under the lower temperature conditions, ~200 ^{o}C, in Carlin-type and epithermal deposit is a surface and kinetically controlled process that resulted in formation of polycrystalline, often nanoscale, aggregates of As-rich Fe-deficient pyrite (Fleet and Mumin, 1997; Palenik et al., 2004; Deditius et al., 2008). Thus, such As-rich nanodomains may incorporate higher amounts of Au than pristine coarse-grained pyrite due to high surface to volume ratio. These constraints were supported by first principles calculations by Reich and Becker (2006) that revealed ordering of As in the pyrite structure with decreasing temperature from ~475 ^{o}C, a temperature characteristic for the Au deposition in porphyry, to ~275 ^{o}C, a temperature characteristic for epithermal deposits (Table A.1). Fully ordered but unknown cubic nanodomains of arsenopyrite were predicted at the solid solution limit for As in pyrite, i.e., ~6 wt. %. Also, progressive cooling that lead to As ordering in pyrite might cause phase separation and exsolution of As-rich domains enriched with Au, previously reported as stacking faults (Simon et al., 1999a).

The presence or absence of arsenopyrite associated with pyrite seems to have no impact on the concentrations of Au in the latter one, and statistically arsenopyrite contains higher amount of Au in all types of ore deposits (Cook and Chryssoulis, 1990; Arehart et al., 1993; Vaughan and Kyin, 2004; Reich et al., 2005; Wagner et al., 2007; Large et al., 2007; Sung et al., 2009; Cook et al., 2013). Furthermore no experimental data is available on the

partitioning of As between arsenopyrite and pyrite. Despite this fact, there seems to be no correlation between the As-bearing growth zones of arsenopyrite-pyrite assemblages (Morey et al., 2008). This suggests a limited (if any) effect of arsenopyrite on As in the pyrite structure; although, more detailed research are needed.

Mobilization of Au and As from the pyrite structure, and thus a decrease in their Au and As content, may also be related to the formation of low-temperature melts during the transition from greenschist to amphibolite facies. This phenomenon may be particularly important for pyrite grains that contain micro- and nanoparticulate sulfosalts (Tomkins et al., 2007), as reported for pyrite from epithermal deposits (Deditius et al., 2011a). It was documented that amorphous NPs of As-Fe-S (i.e., melt) were formed at about ~320 ^{o}C, in pyrite from the high-sulfidation, epithermal Pueblo Viejo deposit (Deditius et al., 2009b). Formation of Au and As bearing melts at this temperature will depend on the relative proportion between As and Fe, as noted on the binary and ternary diagrams for the Fe-As-S system. In the As-S system, S-enriched liquid forms at the temperatures as low as 281 ^{o}C (Raghavan, 1988). In addition, it was shown that Au and As preferentially partition into multi-metallic NPs in pyrite that may be susceptible to melting at temperatures below 250 ^{o}C (Deditius et al., 2011a), especially when Bi is present (Tomkins et al., 2007).

5.6 Partitioning of Au and As into pyrite

One key question is whether pyrite records the As:Au ratio of the ore fluid from which it precipitated. Deditius et al. (2009a) and more recently Reich et al. (2013) have proposed that Au-As-Cu compositional features in pyrite may reflect periodic changes in hydrothermal fluid compositions that are recorded in complex zoning during epithermal Au and porphyry Cu mineralization. In the absence of experimentally-determined fluid/pyrite partition

coefficients for Au and As, we have tested this hypothesis by plotting compositions of pyrite from porphyry Cu and epithermal Au deposits with published Au and As concentrations in coexisting fluids including fluid inclusions, subaerial and subaquatic fumaroles, and volcanic precipitates (Fig. 10). Concentration data in pyrite and hydrothermal ore fluids reveal a relatively good correspondence in Au-As compositional space (Fig. 10). In the absence of post-depositional re-equilibration or metamorphism, these data suggest that pyrite can preserve or register the Au/As ratio of hydrothermal ore fluids.

Kouzmanov et al. (2010) compared Au and As contents in pyrite and associated fluid inclusions. Pyrite compositions from epithermal veins at the Rosia-Poieni porphyry Cu-Au deposit revealed high Au:As ratios ranging from 1:1 to 1:10 (grey triangles, Fig. 10). The amounts of As (0.6-1.3 ppm) in liquid+vapour type fluid inclusions are lower and/or equal, to the measured amounts in pyrite, i.e., 0.8-2.3 ppm of As. The content of Au in this type of fluid inclusions (0.1-3.4 ppm) matches the amounts of Au in pyrite (1-2.2 ppm Au) (Fig. 10). However, concentrations of Au in vapour-rich and particularly in brine-rich inclusions are equal to or higher, 0.4-11.4 ppm and 2.4-41 ppm, respectively. This leads to pyrite/vapour partition coefficients of ~0.35 for Au and pyrite/brine coefficients of ~0.13. In contrast, partition coefficients for As are ~0.2 for pyrite/vapour, and ~0.02 for pyrite/brine. These values suggest that Au and As are preferentially concentrated in the ore fluid relative to pyrite. The high concentrations of Au measured in brine and vapour-rich fluid inclusions match the highest amounts of Au measured in pyrite from the Ok-Tedi porphyry Cu-Au deposit (Table 3) and in pyrite from Dexing porphyry Cu porphyry deposit (Reich et al., 2013). These highest amounts of Au from Dexing correlate with the presence of nanoparticulate Au, as determined by SIMS depth profiling (Reich et al., 2013). Analyses of brine-rich fluid inclusions in pyrite plot close to the solubility limit of Au for pyrite (Fig. 10), confirming that Au-As contents of pyrite may be used to predict quantitatively fluid

saturation with respect to Au^0 (or Au-bearing minerals) during pyrite formation, as Reich et al. (2005) previously suggested. In fact, Kouzmanov et al. (2010) showed that some of their analyses were contaminated by trapped solid inclusions containing Au and As (Figs. 9 and 10 therein). In addition, analyses of As and Au in synthetic fluid inclusions trapped at high-temperature (800 ^{o}C) under S-free *vs*. S-bearing conditions (Simon et al., 2007) also plot within the range of the highest concentrations of As and Au noted in pyrite from porphyry Cu deposits (Fig. 10). The preferential partitioning of As and Au into the magmatic vapour above 450-550 ^{o}C (Pokrovski et al. 2002b), and the higher amounts of these elements in fluid inclusions than in pyrite, suggest that only a fraction of the Au and As carried by the ore fluid is consumed by pyrite in porphyry systems, while the rest of As and Au may be transported into the shallower epithermal level.

Figure 7c clearly demonstrates an increase in the concentrations of Au and As in pyrite during the transition from porphyry to epithermal environments. This observation agrees relatively well with preferential partitioning of Au and As into a vapour phase during segregation from a deep magmatic hypersaline liquid (Heinrich, 2005). Numerous studies have confirmed that Au^+ (Benning and Seward, 1996; Fleet and Knipe, 2000) and As^{3+} (Pokrovski et al., 2002a and b) are the dominant species in hydrothermal fluids under conditions representative of the deposits discussed here. At temperatures below 150 ^{o}C, the behaviour of As in ore fluids is controlled by formation of As_2S_3 phases, while at $T > 200$ ^{o}C the formation of sulfosalts and sulfides like arsenopyrite and arsenian pyrite exert a significant control on As (Pokrovsky et al., 2002a). The data presented here show that Au-As compositions of pyrite match closely the proportion of As and Au in the hydrothermal fluids and confirm the previous predictions that arsenian pyrite acts as a one of major phases controlling As geochemistry in hydrothermal systems at temperatures of > 150 ^{o}C (Pokrovski et al., 2002a; Reich et al., 2005).

As noted previously, the high-concentrations of Au in pyrite from low-temperature, epithermal deposits and partly from Carlin-type deposits suggest supersaturation of Au in the mineralizing fluid. It is important to note that the type of Au-complex in the fluid will promote or decrease the probability of formation of nanoparticulate Au. If Au is delivered as $As(HS)^0$ complexes, then it is likely that it will be incorporated into the As-pyrite as Au^+ (Cardile et al., 1993). In contrast, reduction of Au^+ to Au^0 will be favoured when this metal is delivered as Au-Cl complexes to the surface of pyrite and other sulfides (e.g., Hyland and Bancroft, 1989; Eggleston and Hochella, 1991). Therefore, the fact that the majority of Au-As analyses from various types of ore pyrites plot below the solubility limit is in agreement with the dominant role of sulfur in Au complexation in ore deposits (Fig. 1).

7. SUMMARY AND CONCLUSIONS

This work shows that the coupled geochemistry of Au and As in pyrite is a ubiquitous phenomenon in wide range of hydrothermal and diagenetic environments. The solid solubility limit of Au in arsenian pyrite defined by an Au/As ratio of 0.02 (Reich et al., 2005) is independent of the geochemical environment of pyrite formation and depends on the crystal-chemical properties of pyrite and post-deposition alteration (Fig. 1). The distribution of most analyses below this solubility limit suggests that Au-bearing fluids are largely undersaturated with respect to native Au, and that Au^{1+} is the dominant form of Au in arsenian pyrite from ore deposits. The solubility limit can be disturbed as a result of complex recrystallization histories, high-temperature alteration, or cooling (e.g., in orogenic or metamorphosed VHMS deposits) leading to Au mobilization and growth of post-depositional Au NPs (cooling: vertical trajectory and heating: horizontal trajectories in Figure 11). Therefore, lower amounts of Au are hosted by arsenian pyrite as outlined by a limit of C_{Au} =

$0.004 \cdot C_{As} + 2 \cdot 10^{-7}$ for these deposits. This explains the presence of nanoparticulate Au at lower Au/As ratios than in systems where metamorphic perturbations are absent

Our results indicate that the coupled geochemistry of Au and As in pyrite in ore deposits is defined by two major trends that obey the solubility limit (Reich et al., 2005): (i) pyrite from Carlin-type and orogenic deposits, displaying wedged-shaped zones where pyrite geochemistry is largely controlled by fluid-rock interactions (e.g., sulfidation of wall-rock); and (ii) pyrite from porphyry–to-epithermal deposits whose composition registers and preserves the Au/As signature of ore fluids (Figs. 5-8). This suggests that massive precipitation of Au-bearing arsenian pyrite in porphyry and epithermal environments plays an unforseen role in modifying the Au-As concentrations of hydrothermal ore fluids. In Au-As space, the process of Au-As incorporation into pyrite from an ore fluid will proceed diagonally under isothermal equilibrium (Fig. 11). Under these conditions, the Au-As ratios in arsenian pyrite from ore deposits will preserve the Au-As ratio of the fluid and therefore can be used as a monitor for hydrothermal fluid evolution.

Acknowledgements

The authors are indebted to Richard Goldfarb, Nigel Cook and Robert Linnen and Associate Editor Ed Ripley for their insightful comments that greatly improved the manuscript. Support for this study was provided by NSF EAR 052093 to Utsunomiya and Kesler. Martin Reich thanks support by FONDECYT grants 11070088 and 1130030, and additional support from FONDAP project no. 15090013. Financial support (Grant-in-Aid for Young Scientists) was provided by Japan Society of Promotion of Science (JSPS) to Utsunomiya. The authors are grateful to Carl Henderson for help with EMPA analyses conducted at the Electron Microbeam Analysis Laboratory (EMAL) at the University of Michigan. We also thank to Grigore Simon and Lloyd McEvans of Newmont Gold Corporation for samples from

Yanacocha, and Mark Reed for samples from Butte.

REFERENCES

Agangi A., Hofmann A. and Przybylowicz W. (2014) Trace element zoning of sulfides and quartz at Sheba and Fairview gold mines: Clues to Mesoarchean mineralisation in the Barberton Greenstone Belt, South Africa. *Ore Geol. Rev.,* **56**, 94-114.

Agangi A., Hofman A. and Wohlgemuth-Uberwasser C.C. (2013) Pyrite zoning as a record of mineralization in the Ventersdorp contact reef, Witwatersrand Basin, South Africa. *Econ. Geol.* **108**, 1243-1272.

Ahmad M., Solomon M. and Walshe J.L. (1987) Mineralogical and geochemical studies of the Emperor gold telluride deposit, Fiji. *Econ. Geol.* **82**, 345-370.

An F., Zhu Y. (2010) Native antimony in the Baogutu gold deposit (west Junggar, NW China): Its occurrence and origin. *Ore Geol. Rev.* **37**, 214-223.

Arehart G.B., Chryssoulis S.L. and Kesler S.E. (1993) Gold and arsenic in iron sulfides from sediment-hosted disseminated gold deposits: implications for depositional processes. *Econ. Geol.* **88**, 171-185.

Ashley P.M., Creagh C.J. and Ryan C.G. (2000) Invisible gold in ore mineral concentrates from the Hillgrove gold-antimony deposit, NSM, Australia. *Miner. Deposita* **35**, 285-301.

Barker S.L.L., Hickey K.A., Cline J.S., Dipple G.M., Kilburn M.R., Vaughan J.R. and Longo A.A. (2009) Uncloaking invisible gold: Use of nano-SIMS to evaluate gold, trace elements, and sulphur isotopes in pyrite from Carlin-type gold deposits. *Econ. Geol.* **104**, 897-904.

Barkov A.Y., Halkoaho T.A.A., Laajoki K.V.O., Alapieti T.T. and Peura R.A. (1997) Ruthenian pyrite and nickeloan malanite from the Imandra layered complex, northwestern Russia. *Can. Mineral.* **35**, 887-897.

Barnicoat A.C., Henderson I.H.C., Knipe R.J., Yardley B.W.D., Napier R.W., Fox N.P.C., Kenyon A.K., Muntingh D.J., Strydom D., Winkler K.S., Lawrence S.R. and Cornford C. (1997) Hydrothermal gold mineralization in the Witwatersrand basin. *Nature* **386**, 820-824.

Barrie C.D., Boyce A.J. Boyle A.P., Williams P.J. Blake K., Ogawara T., Akai J. and Prior D.J. (2009) Growth controls in colloform pyrite. *Am. Mineral.* **94**, 415-429.

Barton E.S. and Hellbauer D.K. (1996) Trace-element and U-Pb isotope compositions of pyrite types in the Proterozoic Black Reef, Transvaal Sequence, South Africa: Implications on genesis and age. *Chem. Geol.* **133**, 173-199.

Bayliss P. (1989) Crystal chemistry and crystallography of some minerals within the pyrite group. *Am. Miner.* **74**, 1168-1176.

Becker U., Rosso K.M. and Hochella Jr., M.F. (2001) The proximity effect on semiconducting mineral surfaces: A new aspect of mineral surface reactivity and surface complexation theory? *Geochim. Cosmochim. Acta* **65**, 2641-2649.

Bell P.D., Gomez J.G., Loayza C.E. and Pinto R.M. (2004) Geology of the gold deposit of the Yanacocha deposit, northern Peru. *Australasian Institute of Mining and Metallurgy Publication Series* **5**, 105-115.

Benning L.G. and Seward T.M. (1996) Hydrosulfide complexing of Au (I) in hydrothermal solutions from 150-400^{o}C and 500-1500 bar. *Geochim. Cosmochim. Acta* **60**, 1849-1871.

Bostick B.C. and Fendorf S. (2003) Arsenite sorption on troilite (FeS) and pyrite (FeS_2). *Geochim. Cosmochim. Acta* **67**, 909-921.

Brown S.M., Johnson C.A., Watling R.J. and Premo W.R. (2003) Constraints on the composition of ore fluids and implications for mineralising events at the Cleo gold deposit, Eastern Goldfields Province, Western Australia. *Austral. J. Earth Sci.* **50**, 19-38.

Cardile C.M., Cashion J.D., McGrath A.C., Renders P. and Seward T.M. (1993) ^{197}Au

Mössbauer study of Au_2S and gold adsorbed on to As_2S_3 and Sb_2S_3 substrates. *Geochim. Cosmochim. Acta* **57**, 2481-2486.

Cepedal A., Mrtín-Izard A., Reguilón R., Rodrígues-Pevida L., Spiering E. and González-Nistal S. (2000) Origin an evolution of the calcic and magnesian skarns hosting the El Balle-Boinás copper-gold deposit, Asturias (Spain). *J. Geochem. Explor.* **71**, 119-151.

Cepedal A., Fuertes-Fuente M., Martin-Lizard A., González-Nistal S. and Barrero M. (2008) Gold-bearing As-rich pyrite and arsenopyrite from the El Valle gold deposit, Asturias, northwestern Spain. *Can. Mineral.* **46**, 233-247.

Chen J.-H., Li Y.-Q., Zhong S.-P. and Guo J. (2013) DFT simulation of the occurrences and correlation of gold and arsenic in pyrite. *Am. Mineral.* **98**, 1765-1771.

Chouinard A., Paquette J. and Williams-Jones A.E. (2005a) Crystallographic controls on trace-element incorporation in auriferous pyrite from the Pascua epithermal high-sulfidation deposit, Chile-Argentina. *Can. Miner.* **43**, 951-963.

Chouinard A., Williams-Jones A.E., Leonardson R.W., Hodgson C.J., Silva P., Téllez C., Vega J. and Rojas F. (2005b) Geology and genesis of the multistage high-sulfidation epithermal Pascua Au-Ag-Cu deposit, Chile and Argentina. *Econ. Geol*. **100**, 463-490.

Chowdhurry T.R., Basu G.K., Mandal B.K., Biswas B.K., Samanta G., Chowdhurry U.K., Chanda C.R., Lodh D., Roy S.L., Saha K.C., Roy S., Kabir S., Quamruzzaman Q. and Chakraborti D. (1999) Arsenic poisoning in the Ganges delta. *Nature* **401**, 545-546.

Ciobanu C.L., Cook N.J., Utsunomiya S., Pring A. and Green L. (2011) Focussed ion beam-transmission electron microscopy applications in ore mineralogy: Bridging micro- and nanoscale observations. *Ore Geol. Rev.* **42**, 6-31.

Ciobanu C.L., Cook N.J., Utsunomiya S., Kogagwa M., Green L., Gilbert S. and Wade B. (2012) Gold-telluride nanoparticles in arsenic-free pyrite. *Am. Mineral.* 97, 1515-1518.

Cline J.S. (2001) Timing of gold and arsenic sulfide mineral deposition at the Getchell

Carlin-type gold deposit, North-Central Nevada. *Econ. Geol.* **96**, 75-89.

Cline J.S., Hofstra A.H., Muntean J.L., Tosdal J.M. and Hickey K.A. (2005) Carlin-type gold deposits in Nevada: Critical geologic characteristics and viable models. *Economic Geology 100th Anniversary Volume*, **100**, 451-484.

Cook N.J. and Chryssoulis S.L. (1990) Concentrations of "invisible gold" in the common sulfides. *Can. Miner.* **28**, 1-16.

Cook N.J., Ciobanu C.L. and Mao J. (2009) textural controls on gold distribution in As-free pyrite from the Dongping, Huangtuliang and Hougou gold deposits, North china Craton (Hebei Province, China). *Chem. Geol.* **264**, 101-121.

Cook N.J., Halls C. and Boyle A.P. (1993) Deformation and metamorphism of massive sulphides at Sulitjema, Norway. *Mineral. Mag.* **57**, 67-81.

Craig J.R. and Vokes F.M. (1993) The metamorphism of pyrite and pyritic ores: an overview. *Mineral. Mag.* **57**, 3-18.

Craig J.R., Vokes F.M. and Solberg T.N. (1998) Pyrite: physical and chemical textures. *Mineral. Deposita.* **34**, 82-101.

Currie K.L., Van Staal C.R., Peter J.M and Rogers N. (2003) Conditions of metamorphism of the main massive sulphide deposits and surrounding rocks in the Bathurst Mining Camp. *In* Massive sulphide deposits in the Bathurst Mining Camp, New Brunswick and Northern Maine. Goodfellow S.R., McCutcheon S,R, and Peter J.M. Eds. *Econ. Geol. Monogr.* **11**, 65-78.

Cygan G.L. and Candela P.A. (1995) Preliminary study of gold partitioning among pyrrhotite, pyrite, magnetite, and chalcopyrite in gold-saturated chloride solutions at 600° to 700°C, 140 MPa (1400 bars). *Mineralogical Association of Canada Short Course* **23**, 129-137.

Deditius A.P., Utsunomiya S., Renock D., Ewing R.C., Ramana C.V., Becker U. and Kesler S.E. (2008) A proposed new type of arsenian pyrite: Composition, nanostructure and

geological significance. *Geochim. Cosmochim. Acta* **72**, 2919-2933.

Deditius A.P., Utsunomiya S., Ewing R.C., Chryssoulis S.L., Venter D. and Kesler S.E. (2009a) Decoupled geochemical behaviour of As and Cu in hydrothermal systems. *Geology* **37**, 707-710.

Deditius A.P., Utsunomiya S., Ewing R.C. and Kesler S.E. (2009b) Nanoscale "liquid" inclusions of As-Fe-S in arsenian pyrite. *Am. Mineral.* **94**, 391-394.

Deditius A.P., Utsunomiya S., Kesler S.E., Reich M. and Ewing R.C. (2011a) Trace elements nanoparticles in pyrite. *Ore Geol. Rev.*, **42**, 32-46.

Deditius A.P., Kesler S.E., Utsunomiya S., Reich M. and Ewing R.C. (2011b) Structural and chemical discontinuities in pyrite. *Proceedings of the 11th SGA Biennial Meeting, Chile,* Antofagasta: Univ. Catholica Norte, 2011, pp. XXX-XXX.Deol S., Deb M., Large R.R. and Gilbert S. (2012) LA-ICPMS and EMPA studies of pyrite, arsenopyrite and loellingite from the Bhukia-Jagpura gold prospect, southern Rajasthan, India: implications for ore genesis and gold remobilization. *Chem. Geol.* **326-327**, 72-87.

Dinan T.E., Jou W.-F. and Cheh H.Y. (1989) Arsenic uptake onto gold substrate. *J. Electrochem. Soc.* **136**, 3284-3287.

Ding Z., Zheng B., Long J., Belkin H.E., Finkelman R.B., Chen C., Zhou D. and Zhou Y. (2001) Geological and geochemical characteristics of high arsenic coals from endemic arsenosis areas in southwestern Guizhou Province, China. *App. Geochem.* **16**, 1353-1360.

Distler V.V., Yudovskaya M.A., Mitrofanov G.L., Prokofev V.Y. and Lishnevskiy E.N. (2004) Geology, composition and genesis of the Sukoi Log noble metals deposit, Russia. *Ore Geol. Rev.* **24**, 7-44.

Eggleston C.M. and Hochella M.F. (1991) Scanning tunnelling microscopy of galena (100) surface oxidation and sorption of aqueous gold. *Science* **254**, 983-986.

Emsbo P., Hofstra A.H., Lauha E.A., Griffin G.L. and Hutchinson R.W. (2003) Origin of

high-grade gold ore, source of ore fluid components, and genesis of the Miekle and neighboring Carlin-type deposits, Northern Carlin Trend, Nevada. *Econ. Geol.* **98**, 1069-1105.

Farquhar J., Peters M., Johnston D.T., Strauss H., Masterson A., Wiechert U. and Kaufman A.J. (2007) Isotopic evidence for Mesoarchean anoxia and changing atmospheric sulphur chemistry. *Nature* **449**, 706-709.

Farquhar M.L, Charnock J.M., Livens F.L. and Vaughan D.J. (2002) Mechanism of arsenic uptake from aqueous solution by interaction with goethite, lepidocrocite, mackinawite, and pyrite: An X-ray absorption spectroscopy study. *Environ. Sci. Technol.* **36**, 1757-1762.

Fleet M.E. and Mumin A.H. (1997) Gold-bearing arsenian pyrite and marcasite and arsenopyrite from Carlin Trend gold deposits and laboratory synthesis. *Am. Miner.* **82**, 182-193.

Fleet M.E. and Knipe S.W. (2000) Stability of native gold in H-O-S fluids at 100-400^{o}C and high H_2S content. *J. Sol. Chem.* **29**, 1143-1157.

Foster A.R., Williams P.J. and Ryan C.G. (2007) Distribution of gold in hypogene ore at the Ernest Henry iron oxide copper-gold deposit, Cloncurry District, NW Queensland. *Exploration and Mining Geology* **16**, 125-143.

Frimmel H.E. (2005) Archean atmospheric evolution: evidence from the Witwatersrand gold fields, South Africa. *Earth-Science Rev.* **70**, 1-46.

Frimmel H.E., Groves D.I., Kirk J., Ruiz J., Chesley J. and Minter W.E.L. (2005) The formation and preservation of the Witwatersrand goldfields, the largest gold province in the world. *Economic Geology 100th Anniversary Volume*, **100**, 769-797.

Garnier V., Malo M., Dubé B., Chagnon A. and Beaudoin G. (2007) Carlin-type gold mineralization at Saint-André-de-Ristigouche, Gaspé Peninsula (Québec), Canadian

Appalachians. *Miner. Deposita* **42**, 639-662.

Giles D., Betts P.G. and Lister G.S. (2004) 1.8-1.5-Ga links between the North and South Australia Cratons and the Early-Middle Proterozoic configuration of Australia. *Tectonophysics* **380**, 27-41.

Goldfarb R.J., Baker T., Dubé B., Groves D.I., Hart C.J.R. and Gosselin P. (2005) Distribution, character and genesis of gold deposits in metamorphic terranes. *Economic Geology 100th Anniversary Volume*, **100**, 407-450.

Griffin W.L., Ashley P.M., Ryan C.G., Sie S.H. and Suter G.F. (1991) Pyrite geochemistry in the North Arm epithermal Ag-Au deposit, Queensland, Australia: A proton-microprobe study: *Can. Mineral.*, **29**, 185-198.

Hannington M., Herzig P., Scott S., Thompson G., and Rona P. (1991) comparative mineralogy and geochemistry of gold-bearing sulphide deposits on the mid-ocean ridges. *Marine Geology* **101**, 217-248.

Harms U. (2009) Nickleoan pyrite from Prangenhau quarry, Niedelberg area, Germany – A short communication. *Chemier der Erde* **69**, 279-285.

Harvey B., Myers S. and Klein T. (2004) Yanacocha gold district, northern Peru, Pacific Rim Congress, Bali, Indonesia, 1999, *Australasian Institute of Mining and Metallurgy, Proceeding* **5**, 445-459.

Hayba D.O., Bethke P.M., Heald P. and Foley N.K. (1986) Geologic, mineralogy, and geochemical characteristic of volcanic-hosted epithermal precious-metal deposits. *Rev. Econ. Geol.* **2**, 129-167.

Heinrich C.A. (2005) The physical and chemical evolution of low-salinity magmatic fluids at the porphyry to epithermal transition: a thermodynamic study. *Mineral. Deposita.* **39**, 864-889.

Heinrich C.A., Gunther D., Audetat A., Urlich T. and Frischknecht R. (1999) Metal

fractionation between magmatic brine and vapour, determined by microanalysis of fluid inclusions. *Geology* **27**, 755-758.

Hofmann A., Bekker A., Rouxxel O., Rumble D. and Master S. (2009) Multiple sulfur and iron isotope composition of detrital pyrite in Archean sedimentary rocks: A new tool for provenance analysis. *Earth Planet. Sci. Lett.* **286**, 436-445.

Ho S.E., McQeen K.G., McNaughton N.J. and Groves D.I. (1995) Lead isotope nsystematic and pyrite trace elements geochemistry of two granitoid-associated mesothermal gold deposit in the southeastern Lachlan fold belt. *Econ. Geol.* **90**, 1818-1830.

Hofstra A.H. and Cline J.S. (2000) Characteristics and Models for Carlin-Type Gold Deposits. *SEG Reviews* **13**, 163-220.

Hough, R., Reich, M., and Noble, R. (2012) Noble Metal Nanoparticles in Ore Systems. Nature's Nanostructures. Amanda S. Barnard and Haibo Guo (Eds.), Pan Stanford Publishing Pte. Ltd. ISBN 978-981-4316-82-8 (Hardcover), 978-981.

Huston D.L., Sie S.H., Suter G.F., Cooke D.R. and Both R.A. (1995) Trace elements in sulfide minerals from Eastern Australian volcanic-hosted massive sulfide deposits: Part I: Proton microprobeb analyses of pyrite, chalcopyrite, and sphalerite, and Part II. Selenium levels in pyrite: Comparison with $\delta^{34}S$ values and implications for the source of sulfur in volcanogenic hydrothermal systems. *Econ. Geol.* **90**, 1167-1196.

Hyland M.M. and Bancroft G.M. (1989) Au XPS study of gold deposition at low temperatures on sulphide minerals: Reducing agents. *Geochim. Cosmochim. Acta* **53**, 367-372.

Ingham E.S., Cook N.J., Cliff J., Ciobanu C.L., and Huddleston A. (2014) A combined chemical isotopic and microstructural study of pyrite from roll-front uranium deposits, Lake Eyre Basin, South Australia. *Geochim. Cosmochim. Acta* **125**, 440-465.

Jia Y., Li X. and Kerrich R. (2000) A fluid inclusion study of Au-bearing quartz vein systems

in the central and north Deborah deposit of the Bendigo gold field, central Victoria, Australia. *Econ. Geol.* **95**, 467-494.

Johan Z., Marcoux E. and Bonnemaison M. (1989) Arsénopyrite aurifère : mode de substitusion de Au dans le structure de FeAsS. *C.R. Acad. Sci. Paris* **308**, Sér. II, 185-191.

John D.A., Hofstra A.H., Fleck R.J., Brummer J.E. and Saderholm E.C. (2003) Geologic setting and genesis of the Mule Canyon low-sulfidation epithermal gold-silver deposit, north-central Nevada. *Econ. Geol.* **98**, 425-463.

Koglin N., Frimmel H.F., Lawrie Minter W.E. and Brätz H. (2010) Trace-element characteristics of different pyrite types in Mesoarchean to Paleoproterozoic placer deposits. *Miner. Deposita* **45**, 259-280.

Kouzmanov K., Pettke T. and Heinrich C.A. (2010) Direct analysis of ore-precipitating fluids: Combined IR microscopy and LA-ICP-MS study of fluid inclusions in opaque ore minerals. *Econ. Geol.* **105**, 351-373.

Large R.R., Maslennikov V.V., Robert F., Danyushevsky L. and Chang Z. (2007) Multistage Sedimentary and metamorphic origin of pyrite and gold in the giant Sukhoi Log deposit, Lena gold province, Russia. *Econ. Geol*., **102** 1233-1267.

Large R.R., Danyushevsky L., Hollit C., Maslennikov V.V., Meffre S., Gilbert S., Bull S., Scott R., Emsbo P., Thomas H., Singh B. and Foster J. (2009) Gold and trace elements zonation in pyrite using Laser Imaging Technique: Implifications for the timing of gold in orogenic and Carlin-Style sediment-hosted deposits: *Econ. Geol*., **104**, 635-668.

Law J.D.M. and Phillips G.N. (2005) Hydrothermal replacement model for Witwatersrand gold. *Economic Geology 100th Anniversary Volume 1905-2005* **100**, 799-812.

Lentz D.R. (2002) Sphalerite and arsenopyrite at the Brunswick No. 12 massive-sulfide deposit, Bathrust camp, New Brunswick: Constraints on P-T evolution. *Can. Miner.* **40**, 19-31.

Lorand J.-P. and Alard O. (2011) Pyrite tracks assimilation of crustal sulphur in Pyrenean peridotites. *Miner. Petrol.* **101**, 115-128.

Lorand J.-P. and Alard O. (2011) Pyrite tracks assimilation of crustal sulphur in Pyrenean peridoties. *Miner. Petrol.***, 101**, 115-128.

Maddox L.M., Bancroft G.M., Scaini M.J. and Lorimer J.W. (1998) Invisible gold Comparison of Au deposition on pyrite and arsenopyrite. *Am. Mineral.* **83** 1240-1245.

Mao J.W., Li Y.Q., Goldfarb R., He Y. and Zaw K. (2003) Fluid inclusion and noble gas studies of the Dongping gold deposit, Hebei Province, China: A mantle connection for mineralization? *Econ. Geol.* **98**, 517-534.

Mao J., Zhang J., Piranjo F., Ishiyama D., Su H., Gou C. and Chen Y. (2011) Porphyry Cu-Au-Mo-epithermal Ag-Pb-Zn-distal hydrothermal Au deposits in the Dexing area, Jiangxi province, East China-A linked ore system. *Ore Geol. Rev.* **43**, 203-216.

Mark G., Oliver N.H.S., Williams P.J., Valenta R.K. and Crookes R.A. (2000) The evolution of the Ernest Henry hydrothermal system. In Porter T.M. ed. Hydrothermal iron oxide copper-gold and related deposits: A global perspective: Adelaide, Porter GeoConsultancy Publishing, **1**, 123-136.

Mark G., Williams P.J., Oliver N.H.S., Ryan C.G. and Mernagh T. (2005) Fluid inclusion and stable isotope geochemistry of the Ernest Henry iron oxide copper-gold deposit, Queensland, Australia. In Mao J. and Bierlien F.P. eds. Mineral deposit research: Meeting the global challenge: Berlin, Springer, p. 785-788.

Masslennikov V.V., Masslennikova S.P., Large R.R. and Danyushevsky L.V. (2009) Study of trace element zonation in vent chimneys from the Silurian Yaman-Kasy volcanic-hosted massive sulphide deposit (Southern Urals, Russia) using laser ablation-inductively coupled plasma mass spectrometry (LA-ICPMS). *Econ. Geol.* **104**, 1111-1141.

McKibben M.A. and Elders W.A. (1985) Fe-Zn-Cu-Pb mineralization in the Salton Sea

geothermal system, Imperial Valley, California. *Econ. Geol.* **80**, 539-559.

McClenaghan S.H., Lentz D.R. and Cabri L.J. (2004) Abundance and speciation of gold in massive sulfide of the Bathrust mining camp, New Brunswick, Canada. *Can. Miner.* **42**, 851-871.

McLean P.J. and Fleet M.E. (1989) Detrital pyrite in Witwatersrand gold fields of South Africa; evidence from truncated growth banding. *Econ. Geol.* **84**, 2008-2011.

Mikhlin, Y., Romanchenko, A., Likhacki, M., Karacharov, A., Erenburg, S. and Trubina, S. (2011) Understanding the initial stages of metals precipitation: Nanoscale metallic and sulphide species of gold and silver on pyrite surfaces. *Ore Geol. Rev.*, **42**, 47-54.

Morey A.A., Tomkins A.G., Bierlin F.P., Wienberg R.F. and Davidson G.J. (2008) Bimodal distribution of gold in pyrite and arsenopyrite: Examples from the Archean Boorara and Bardoc shear systems, Yilgarn craton, Western Australia. *Econ. Geol.* **103**, 599-614.

Mumin A.H., Fleet M.E. and Chryssoulis S.L. (1994) Gold mineralization in As-rich mesothermal gold ores of the Bogosu-Prestea mining district of the Ashanti Gold Belt, Ghana: remobilization of "invisible" gold. *Mineral. Deposita* **29**, 445-460.

Mumin A.H., Fleet M.E. and Longstaffe F.J. (1996) Evolution of hydrothermal fluids in the Ahanti gold belt, Ghana: Stable isotope geochemistry of carbonates, graphite, and quartz. *Econ. Geol.* **91**, 135-148.

Muntean J.L., Kesler S.E., Russell N. and Polanco J. (1990) Evolution of the Monte Negro acid sulphate Au-Ag deposit, Pueblo Viejo, Dominican-Republic – Importnant factors in the grade development. *Econ .Geol.* **85**, 1738-1758.

Muntean J.L., Cline J.S., Simon A.C. and Longo A.A. (2011) Magmatic-hydrothermal origin of Nevada's Carlin-type gold deposits. *Nature Geoscience* **4**, 122-127.

Okrusch M., Lorenz J.A. and Weyer S. (2007) The genesis of sulphide assemblages in the former Wilhelmine mine, SPassart, Bavaria, Germany. *Can. Mineral.* **45**, 723-750.

O'Shaugnessy, T.A., Barber, H.D., Thompson, D.A. and Heasell, E.L. (1974) The solid solubility of gold in doped silicon by oxide encapsulation. *J. Electrochem. Soc.*, **121**, 1350-1354.

Pačevski A., Moritz R., Kouzmanov K., Marquart K., Živković P. and Cvetković L. (2012) Texture and composition of Pb-bearing pyrite from the Čoka Marin polymetallic deposit, Serbia, controlled by nanoscale inclusions. *Can. Mineral.* **50**, 1-20.

Palenik C.S., Ustunomiya S., Reich M., Kesler S.E., Wang L. and Ewing R.C. (2004) "Invisible" gold revealed: Direct imagining of gold nanoparticles in a Carlin-type deposit. *Am. Miner.* **89**, 1359-1366.

Pals D.W., Spry P.G. and Chryssoulis S. (2003) Invisible gold and tellurium in arsenic-rich pyrite from the Emperor gold deposit, Fiji: Implications for gold distribution and deposition. *Econ. Geol.* **98**, 479-493.

Pass H.E. (2010) Breccia-hosted chemical and mineralogical zonation patterns of the northest zone, Mt. Polley Cu-Ag-Au alkali porphyry deposit, British Columbia, Canada. Ph.D. thesis. University of Tasmania.

Phillips N.G. and Law J.D.M. (2000) Witwatersrand gold fields: geology, genesis, and exploration. *Rev. Econ. Geol.* **13**, 439-500.

Phillipot P., Van Zuilen M., Lepot K., Thomazo C., Farquhar J. and Van Kranendonk M.J. (2007) Early Archean microorganisms preferred elemental sulphur, not sulphate. *Science* **317**, 1534-1537.

Pokrovski G., Gout R., Schott J., Zotov A. and Harrichoury J.-C. (1996) Thermodynamic properties and stoichiometry of As(III) hydroxide complexes at hydrothermal conditions. *Geochim. Cosmochim. Acta* **60**, 737-749.

Pokrowski G.S., Kara S. and Roux J. (2002a) Stability and solubility of arsenopyrite, FeAsS, in crustal fluids. *Geochim. Cosmochim. Acta* **66**, 2361-2378.

Pokrovski G.S., Zakirov I.V., Roux J., Testamale D., Hazeman J.-L., Bychkov A.Y., Golikova G.V. (2002b) Experimental study of arsenic speciation in vapour phase to 500°C: Implications for As transport and fractionation in low-density crustal fluids and volcanic gases. *Geochim. Cosmochim. Acta* **66**, 3453-3480.

Putnis A. (2009) Mineral replacement reactions. *Rev. Mineral. Geochem.* **70**, 87-124.

Qian G., Brugger J., Testamale D., Skiner W. and Pring A. (2012) Formation of As(II)-pyrite during experimental replacement of magnetite under hydrothermal conditions. *Geochim. Cosmochim. Acta* **100**, 1-10.

Raghavan V. (1988) Ternary systems containing iron and sulphur, 360 p. ASM International, Metals Park, Ohio.

Reich M., Kesler S.E., Utsunomiya S., Palenik C.S., Chryssoulis S.L. and Ewing R.C. (2005) Solubility of gold in arsenian pyrite. *Geochim. Cosmochim. Acta* **69**, 2781-2796.

Reich M. and Becker U. (2006) First-principles calculations of the thermodynamic mixing properties of arsenic incorporation into pyrite and marcasite. *Chem. Geol.* **225**, 278-290.

Reich M., Utsunomiya S., Kesler S.E., Wang L.M., Ewing R.C. and Becker U. (2006) Thermal behaviour of metal nanoparticles in geologic materials: *Geology,* **34**, 1033-1036.

Reich M., Deditius A., Chryssoulis S., Li J.W., Ma C.Q., Parada M.A., Barra F., and Mi ttermayr F. (2013) Pyrite as a record of hydrothermal fluid evolution in a porphyry copper system: A SIMS/EMPA trace element study. *Geochim.Cosmochim. Acta* **104**, 42–62.

Richards J.P. and Kerrich R. (1993) The Porgera gold mine Papua New Guinea; magmatic hydrothermal to epithermal evolution of an alcalic-type precious metal deposit. *Econ. Geol.* **88**, 1017-1052.

Rickard D. and Luther III G.W. (2007) Chemistry of iron sulphides. *Chem. Rev.* **107**, 514-562.

Ronacher E., Richards J.P., Reed M.H., Bray C.J., Spooner E.T.C. and Adams P.D. (2004) Characteristics and evolution of the hydrothermal fluid in the north zone high-grade area,

Porgera gold deposit, Papua New Guinea. *Econ. Geol.* **99**, 843-867.

Rosúa F.J.C., Ruano S.M. and Hach-Alí P.F. (2002) The three generations of gold in the Palai-Islica epithermal deposit, southeastern Spain. *Can. Miner.* **40**, 1465-1481.

Rosúa F.J.C., Ruano S.M. and Hach-Alí P.F. (2003) Iron sulfides at the epithermal gold-copper deposit of Palai-Islica (Almería, Spain). *Miner. Mag.* **67**, 1059-1080.

Ruano S.M., Rosúa F.J.C., Hach-Alí P.F., de la Fuente Chacón F. and López E.C. (2000) Epithermal Cu-Au mineralization in the Palai-Islica deposit, Almeria, southeastern Spain: Fluid-inclusion evidence for mixing of fluids as a guide to gold mineralization. *Can Mineral.* **38**, 553-565.

Saunders J.A. (1990) Colloidal transport of gold and silica in epithermal precious-metal systems: Evidence from the Sleeper deposit, Nevada. *Geology*, **18**, 757-760.

Savage K.S., Tingle T.N., O'Day P.A., Waychunas G.A. and Bird D.K. (2000) Arsenic speciation in pyrite and secondary weathering phases, Mother Lode gold district. Tuolumne County, California. *App. Geochem.* **15**, 1219-1244.

Seedorff E., Dilles J.H., Proffett Jr. J.M., Einaudi M.T., Zurcher L., Stavast W.J.A., Johnson D.A. and Barton M.D. (2005) Porphyry deposits: Characteristics and origin of hypogen features. *Economic Geology 100th Anniversary Volume 1905-2005* 251-298.

Seo J.H., Guillong M., and Heinrich C.A. (2009) The role of sulphur in the formation of magmatic-hydrotehrmal copper-gold deposits. *EPSL* **282**, 323-328.

Sibson R.H., Robert F. and Poulsen K.H. (1988) High-angle reverse faults, fluid-pressure cycling, and mesothermal gold-quartz deposits. *Geology*, **16**, 551-555.

Simmons S.F., White N.C. and John D.A. (2005) Geological characteristics of epithermal precious and base metal deposits. *Economic Geology 100th Anniversary Volume 1905-2005* **100**, 485-522.

Simon G., Huang H., Penner-Hahn J.E., Kesler S.E. and Kao L.-S. (1999a) Oxidation state of

gold and arsenic in gold-bearing arsenian pyrite. *Am. Miner.* **84**, 1071-1079.

Simon G., Kesler S.E. and Chryssoulis S. (1999b) Geochemistry and textures of gold-bearing arsenian pyrite, Twin Creeks, Nevada: Implications for deposition of gold in Carlin-type deposits. *Econ. Geol.* **94**, 405-422.

Simon A.C., Pettke T., Candela P.A., Piccoli P.M. and Heinrich C.A. (2007) The partitioning behaviour of As and Au in S-free and S-bearing magmatic assemblages. *Geochim. Cosmochim. Acta* **71**, 1764-1782.

Smedley P.L. and Kinniburgh D.G. (2002) A review of the source, behaviour and distribution of arsenic in natural waters. *App. Geochem.* **17**, 517-568.

Su W., Xia B., Zhang H.T., Zhang X.C. and Hu R.Z. (2008) Visible gold in arsenian pyrite at the Shuiyidong Carlin-type gold deposit, Guizhou, China: implications for the environment and processes of ore formation. *Ore Geol. Rev.* **33** 667-679.

Su W., Heinrich C.A., Pettke T., Zhang X., Hu R. and Xia B. (2009) Sediment-hosted gold deposits in Guizhou, China: Products of wall-rock sulfidation by deep crustal fluids. *Econ. Geol.* **104**, 73-93.

Su W., Zhang H., Hu R., Ge X., Xia B., Chen Y. and Zhu C. (2012) Mineralogy and geochemistry of gold-bearing arsenian pyrite from Shuiyidong Carlin-type gold deposit, Guizhou, China: implications for gold depositional processes. *Miner. Deposita* **47** 653-662.

Sung Y.-H., Brugger J., Ciobanu C.L., Pring A., Skinner W. and Nugus M. (2009) Invisible gold in arsenian pyrite and arsenopyrite from a multistage Archean gold deposit: Sunrise Dam Eastern Goldfields Province, Western Australia. *Miner. Deposita* **44**, 765-791.

Tauson V.L. (1999) Gold solubility in the common gold-bearing minerals: Experimental evaluation and application to pyrite. *Eur. J. Mineral.* **11**, 937-947.

Thomas H.V., Large R.R., Bull S.W., Masslennikov V., Berry R.F., Fraser R., Froud S. and

Moye R. (2011) Pyrite and pyrrhotite textures and composition in sediments, laminated quartz veins, and reefs at Bendigo gold mine, Australia: Insights for ore genesis. *Econ. Geol.* **106**, 1-31.

Tokhomirova V.I., Akhmedzhanova G.M. and Nekrasov I.Y. (1994) An investigation of the effect of arsenic and redox conditions on solubility of gold in halogenide solutions at 200-300^{0}C and a pressure of 50 MPa. *Exp. Geosci.* **3**, 1-9.

Tomkins A.G., Pattison D.R.M. and Frost B.R. (2007) On the initiation of the metamorphic sulfise anatexis. *J. Petrol.* **48**, 511-535.

Urlich T., Günter D. and Heinrich C.A. (1999) Gold concentrations of magmatic brines and the metal budget of porphyry copper deposits. *Nature* **399**, 676-679.

Urlich T., Günter D. and Heinrich C.A. (2001) The evolution of a porphyry Cu-Au deposit, based on LA-ICP-MS analysis of fluid inclusions: Bajo de la Alumbrera, Argentina. *Econ. Geol.* **96**, 1743-1774.

Valásquez G., Béziat D., Salvi S., Siebenaller L., Borisova A.Y., Pokrovski G.B. and de Parseval P. (2014) Formation and deformation of pyrite and implications for gold mineralization in the El Callao District, Venezuela. *Econ. Geol.* **109**, 457-486.

Vaughan J.P. and Kyin A. (2004) Refractory gold ores in Archean greenstones, Western Australia: mineralogy, gold paragenesis, metallurgical characterization and classification. *Mineral. Mag.* **68**, 255-277.

Wagner T. and Boyce A.J. (2006) Pyrite metamorphism in the Devonian Hunsrück slate of Germany: Insights from laser microprobe sulphur isotope analysis and thermodynamic modelling. *Am J. Sci.* **306**, 525-552.

Wagner T., Klemd R., Wenzel T. and Mattsson B. (2007) Gold upgrading in metamorphosed massive sulphide ore deposits: Direct evidence from laser-ablation-incuctively coupled plasma-mass spectrometry analysis of invisible gold. *Geology*, **35**, 775-778.

Winderbaum L., Ciobanu C.L., Cook N.J., Paul M., Metcalfe A. and Gilbert S. (2012) Multivariant analysis of an LA-ICP-MS trace element dataset for pyrite. *Math. Geosci.* **44**, 823-842.

Weir Jr. R.H. and Kerrick D.M. (1987) Mineralogic, fluid inclusion, and stable isotope studies of several gold mines in the Mother Lode, Tuolumne and Mariposa Counties, California. *Econo. Geol.* **82**, 328-344.

Williams-Jones A.E. and Heinrich C.A. (2005) Vapor transport of metals and the formation of magmatic-hydrothermal ore deposits. *Economic Geology 100th Anniversary Volume 1905-2005* **100**, 1287-1312.

Wood B.L. and Large R.R. (2007) Syngenetic gold in western Victoria: occurrence, age and dimensions. *Australian J. Earth Sci.*, **54**, 711-732.

Woodhead J., Hergt J., Meffre S., Large R.R., Danyushevsky L. and Gilbert S. (2009) In-situ Pb-isotope analysis of pyrite by laser ablation (multi-collector and quadrupole) ICPMS. *Chem. Geol.* **262**, 344-354.

Yudovskaya M.A., Distler W., Chaplygin I.V., Mokhov A.V., Trubkin N.V. and Gorbacheva S.A. (2006) Gaseous transport and deposition of gold in magmatic fluid: evidence from the active Kudryavy volcano, Kurile Islands. *Mineral. Deposita* **40**, 828-848.

Zachariáš J., Frýda J., Paterová B. and Mihalievič M. (2004) Arsenopyrite and As-bearing pyrite from the Roudný deposit, Bohemian Massif. *Miner. Mag.* **68**, 31-46.

Zachariáš J., Adamovič J. and Langrová A. (2008) Trace elements chemistry in low-temperature pyrites – an indicator of past changes in fluid chemistry and fluid migration paths (Eger Graben, Czech Republic). *Geologica Carpathica* **59**, 117-132.

Zachariáš J., Paterová B. and Pudilová M. (2009) Mineralogy, fluid inclusion, and stable isotope constraints on the genesis of the Roudný Au-Ag deposit, Bohemian Massif. *Econ. Geol.* **104**, 53-72.

Figure captions

Figure 1. Compilation of pyrite compositions in Au-As space (log-scale, in mol %) (the data sources are listed in the Table A1). Note the wedge-shaped zone (grey solid line), which hosts most of the analyses that plot along the orange arrow marking a positive correlation between Au and As. The blue arrow indicates the trend of increasing Au in As-poor pyrite (Cook et al., 2009). Note that most analyses plot below the solubility limit after Reich et al. (2005).

Figure 2. Composition of pyrite from ore deposits on As-Fe-S ternary. Four different trends show substitution of (i) As for S (As^{1-}-pyrite; blue arrow); (ii) As^{2+} for Fe (As^{2+}-pyrite; green arrow); (iii) As^{3+} for Fe (As^{3+}-pyrite; red arrow); and (iv) divalent metals Me^{2+} for Fe (yellow arrow). The composition of As^{2+}-pyrite (after Qian et al., 2012) was calculated based on the assumption of ideal occupancy of S (66.66 at%). n=2924.

Figure 3. Plot of the EMPA (a-b) and SIMS (c-d; Carlin-type deposits) analyses of pyrite from Carlin-type, epithermal, deposits; this study. (a) and (b) Correlations between As and S and Fe (in at. %), respectively; Note negative correlation between As and S in all samples except "Yanacocha", which correlates negatively with Fe (see Deditius et al., 2008). (c) Positive correlation of Te vs. (Au,Ag,Sb); (d) Positive correlation of (Ag,Sb) vs. Au.

Figure 4. (a) Plot of log Au vs. log As (in mol%) for pyrite analyses. Note the distribution of analytical points into two groups: i) data points (mostly SIMS analyses) that form wedge shaped zone in which concentration of Au increases with As content; and ii) data points (largely EMPA analyses) for which Au concentration does not change with increase of As content; (b) Plot of the SIMS analyses from orogenic gold deposits. Note, that only one group

of analyses reveals a positive correlation between As and Au, and there are no analytical points above the dashed-line limiting the wedge-shape zone. (c) Plot of Au vs. As analyses in pyrite for Carlin-type+epithermal deposits and orogenic Au deposits. Note that pyrite from orogenic Au deposits contain about one order of magnitude less Au for corresponding As contents compared to pyrite from Carlin-type and epithermal deposits; i.e., upper limit ~7500 ppm; dashed lines indicate the Au:As ratios.

Figure 5. Compilation of all pyrite compositions in Au-As space (log-scale, in mol %); dotted lines represent Au:As ratios. (a) Plot of data points against the solubility limit of Au in As-pyrite, with analyses that represent Au in solid solution and/or in NPs. Note that most analyses plot in the wedge-shaped zone below Au:As 1:100. (b) Plot displaying analyses of fluid composition from Shuyindong deposit after Su et al. (2008; 2009; 2012). Note the order of magnitude decrease in Au concentration between the early fluid that delivered the Au and the fluid coeval with pyrite precipitation (dashed, grey arrow). No changes in the As concentrations in the fluid were observed. The cluster of data points of Au-rich As-pyrite, (Au >100 ppm and As >9000 ppm), does not represent any specific locality or textural type of pyrite; it rather represents the large number of EMPA analyses with low detection limits.

Figure 6. Au-As composition of all pyrite analyses from orogenic deposits (in mol %). (a) Two wedge-shaped zones of pyrite analyses (orange dashed line) represent Au NPs). Note similar slope of these zones. Grey arrow indicates trend of analyses of As-poor pyrite from Dongpping (Cook et al., 2009). Note Au NPs below the solubility limit of Au in pyrite (see explanation in the text). (b) Selected analyses of pyrite showing evidence for Au mobilization. The experimental data by Cook et al. (2009) at 320 ^{o}C plot close to and/or below the solubility limit of Au in pyrite. The black arrows indicate analyses that document

Au as a minor component of multimetallic NPs (Sung et al., 2009). (c) Comparison of wedge-shaped zones for pyrite from Carlin-type and orogenic deposits. Note that the wedge-shaped zone (2) of the orogenic deposits is almost completely overlapped by the one representing pyrite from Carlin-type deposits.

Figure 7. Solubility limit of Au in all analysed pyrite from porphyry (a) and epithermal (b) deposits (details in Supplementary information, Table A1). (a) Note relatively low concentrations of Au in pyrite, ≤6 ppm that plot below the solubility limit of Au (Reich et al., 2005); except the analyses of pyrite rich in Au NPs. (b) Plot of Au-rich, ≥0.2 ppm, pyrite analyses from epithermal deposits. Note the high Au:As ratio in pyrite from Rosia Poieni deposit >1:10, and numerous analyses of pyrite representing Au NPs above the solubility limit of Au (Reich et al., 2005); "ss"-stands for solid solution. (c) Increase in Au and As concentrations (dashed, grey arrow) for porphyry and epithermal deposits. Note partial overlap of data points.

Figure 8. Gold and As content in pyrite from other types of deposits. Note (i) very high concentration of Au in pyrite from coal and Witwatersrand deposits plotting completely or partly above the solubility limit, respectively; (ii) all analyses of Au in pyrite from VMS deposits (unless metamorphosed) plot below solubility limit suggesting Au in solid solution in As-pyrite.

Figure 9. Variation of Au (a) and As (b) concentrations (in mol %; log scale) as a function of temperature (^{o}C). Error bars display the standard deviation (1σ) for elemental concentrations and the temperature range for the formation of ore stage pyrite. Error bars that exceed the lower range of X-axis were removed for clarity.

Figure 10. Plot of fluid inclusions analyses (natural and experimental) in Au-As space (log-log scale; in mol %). Note that most of fluid inclusions plot in the area of overlap between epithermal and porphyry pyrite. Note: (i) generally higher concentrations of Au and As in FI than in pyrite from Rosia Poieni deposit; (ii) The experimental data of S-free experiment (Simon et al., 2007) and some analyses of FI (Kouzmanov et al., 2010), plot above the solubility limit of Au, which may suggest supersaturation with respect to Au; see text for further discussion.

Figure 11. Partitioning of Au between hydrothermal fluid and pyrite as a function of As concentration.

Table 1

Table 1. The summary of the EMPA analyses of pyrite from Carlin-type, epithermal, and porphyry deposits (in wt. %). bdl - below detection limit.

Sample	S	Fe	Co	Ni	Cu	Zn	As	Se	Ag	Sb	Te	Au	Hg	Pb	Bi	Total
Detection limits	0.039± 0.003	0.036± 0.003	0.024± 0.002	0.019± 0.001	0.023± 0.001	0.027± 0.001	0.020± 0.003	0.013± 0.01	0.049± 0.002	0.049± 0.005	0.023± 0.001	0.047± 0.002	0.061± 0.003	0.115± 0.008	0.05±0. 008	
CARLIN-TYPE (Twin Creeks) (N=18)																
CTW-197-805																
Min.	47.79	40.91	0.04	bdl	bdl	bdl	0.05	bdl	bdl	bdl	bdl	bdl	bdl	bdl	n.a.	97.15
Max.	53.53	46.17	0.06	bdl	0.34	bdl	7.70	0.04	0.07	1.27	bdl	bdl	bdl	bdl	n.a.	99.90
Mean	50.69± 1.82	43.82± 1.35	0.05± 0.003	bdl	0.14± 0.12	bdl	3.27± 2.48	0.01± 0.009	bdl	0.04± 0.10	bdl	bdl	bdl	bdl	n.a.	98.16± 0.68
PORPHYRY (Butte) (N=53)																
Min.	52.55	45.20	bdl	bdl	bdl	bdl	bdl	bdl	bdl	bdl	bdl	bdl	bdl	bdl	n.a.	98.10
Max.	54.20	46.81	bdl	0.05	0.43	bdl	0.06	bdl	0.05	bdl	bdl	bdl	bdl	bdl	n.a.	100.60
Mean	53.53± 0.25	46.31± 0.34	bdl	bdl	0.04±0. 07	bdl	bdl	bdl	bdl	bdl	bdl	bdl	bdl	bdl	n.a.	100.01±0. 4
EPITHERMAL (Yanacocha) (N=36)																
CHQ 606 N3																
Min.	49.71	38.23	bdl	bdl	bdl	bdl	bdl	bdl	bdl	bdl	bdl	bdl	bdl	bdl	n.a.	96.33
Max.	53.82	46.56	0.06	0.11	0.22	0.15	5.22	0.02	0.05	0.04	0.02	0.45	bdl	4.14	n.a.	100.50
Mean	52.94± 0.93	41.37± 2.54	bdl	0.01± 0.02	0.03± 0.05	0.03± 0.03	3.41± 1.76	0.02± 0.01	bdl	0.02± 0.01	bdl	0.22± 0.14	bdl	0.96± 0.81	n.a.	99.04± 0.87

ACCEPTED MANUSCRIPT

Table 2

Table 2. The summary of SIMS analyses of trace elements in from Carlin-type deposits (in ppm).

Sample		Co	Ni	Cu	As	Se	Ag	Sb	Te	Au
Meikle										
(M-03-04); n=17	Min.	12.75	3.95	15.14	4936.55	0.01	n.d.	n.d.	0.18	0.13
	Max	183.26	116.89	643.20	56776.27	0.04	6.50	3815	1.14	39.70
	Mean	69.00±54.21	37.77±35.55	242.65±182.91	32159.89±16569.59	0.02±0.01	1.50±1.85	930.23±1392.84	0.47±0.24	8.76±13.88
(M-03-08); n=14	Min.	0.30	0.51	324.61	10896.77	0.05	12.74	12.14	0.60	0.75
	Max	14.00	88.55	2035.96	50957.96	33.88	607.08	3721.05	69.86	2522.23
	Mean	3.82±4.60	13.76±22.87	775.87±543.95	33783.81±11926.20	8.29±10.27	150.162±216.99	949.31±1433.06	15.72±25.63	280.43±667.15
(M-03-08B); n=14	Min.	0.35	1.82	22.25	686.34	2.81	n.d.	7.08	0.19	0.32
	Max	61.09	141.68	1103.19	69973.90	28.56	368.24	3564.17	45.52	675.18
	Mean	14.04±17.38	30.76±38.61	532.34±312.52	27028.18±24062.67	12.36±7.68	101.22±129.71	721.26±1084.19	11.52±15.38	194.16±259.80
(M-03-17); n=23	Min.	79.36	156.36	2.82	483.13	5.09	n.d.	7.33	0.04	0.18
	Max	1750.80	4589.51	1265.04	125602.62	40.11	65.90	7298.03	1.89	292.64
	Mean	643.25±456.0	1508.70±1308.69	552.89±401.89	39857.24±37056.13	13.01±8.79	6.76±14.21	1730.48±1831.02	0.72±0.48	99.15±95.62
Rodeo										
R-03-01B; n=5	Min.	8.18	592.03	293.09	2878.85	976.71	169.81	476.67	4.87	2.66
	Max	44.20	3005.70	6346.27	5007.50	3000.68	374.60	834.37	17.78	12.80
	Mean	17.41±15.46	1245.80±996.39	2447.22±2487.66	3591.24±876.83	1904.39±887.96	265.20±96.13	637.32±148.36	10.33±5.33	6.79±4.29
R-03-04; n=9	Min.	20.06	92.6	37.072	538.47	22.03	2.31	96.70	0.38	2.42
	Max	832.11	2271.99	979.68	6483.37	184.21	133.96	542.56	15.73	2146.00
	Mean	368.1±253.1	1233.71±693.95	591±293.54	2976.74±1943.94	80.77±52.68	66.61±48.42	246.48±159.18	8.58±5.21	266.01±705.37
Deep Star										
DS-03-04; n=9	Min.	55.31	32.94	21.72	36	2	n.a.	17.58	0.63	0.24
	Max	215.48	1012.02	1070.68	105162.09	261.34	n.a.	12152.884	20.36	308.69
	Mean	127.46±61.25	353.78±313.41	433.23±347.99	50291.51±40568.58	67.49±86.56	n.a.	4368.49±4547.99	7.34±7.71	84.21±103.32
Betze-Post										
S-03-03; n=10	Min.	1173.62	68.31	6.79	2325.40	10.14	n.d.	n.d.	0.37	0.20
	Max	5002.30	181.66	63.95	4227	13.97	2.08	41.16	2.34	83.13
	Mean	2787.82±1723.85	115.78±58.79	33.23±23.09	1679.78±1673.73	11.83±1.9	0.89±0.77	32.53±12.2	1.17±0.79	22.58±29.26
DP-03-04B; n=13	Min.	86.58	135	233.14	11325.72	35.42	n.a.	1387.45	3.49	36.34
	Max	356.41	586.97	897.20	92171.03	189.41	n.a.	10225.49	31.77	195.46
	Mean	213.75±114.3	271.07±152.67	451.89±215.84	40592.46±29550.09	86.40±43.7	n.a.	4273.83±3119.14	12.3±9.7	92.68±54.91
GS-03-11; n=9	Min.	32.27	51.61	9.22	464.91	5.87	n.a.	39.77	0.25	0.43
	Max	779.2	324.35	519.12	186018.19	38.94	n.a.	1286.04	9.44	33.32
	Mean	224.2±216.69	174.18±84.56	143.39±167.89	38.626.9±65641.48	18.49±12.72	n.a.	409.03±454.15	2.64±3.27	8.44±12.05

Twin Creeks										
CTW-150-950; n=13	Min.	25.88	65.28	17.46	2136.93	4.99	n.a.	37.15	1.42	0.41
	Max	234.24	794.44	248.88	87544.47	35.99	n.a.	310.32	21.08	23.56
	Mean	111.23±75.55	318.55±254.27	115.13±82.25	33520.22±28684.44	18.01±11.93	n.a.	85.16±71.13	9.16±6.79	10.01±7.8
SED082-474; n=32	Min.	4.6	0.7	3.5	402.48	1.45	n.a.	20.14	0.83	0.42
	Max	6733.86	236.31	177.57	48312.7	91.72	n.a.	157.74	15.73	17.86
	Mean	686.41±1307.24	32.52±52.01	43.34±43.64	8350.35±10359.6	11.3±16.19	n.a.	101.77±76.21	4.5±3.77	3.29±3.6
CTW-150-959; n=11	Min.	7.74	9.97	23.97	1252.99	1.42	n.a.	22.85	0.17	n.d.
	Max	348.24	53.64	145.05	60657.34	8.22	n.a.	273.9	6.87	4.09
	Mean	78.81±102	23.57±14.3	96.32±36.98	30144.48±23086.84	3.63±1.82	n.a.	107.43±78.46	3.47±2.96	1.95±1.41
Bald Mountain	Min.	n.a.	15.69	50.07	6781.09	0.24	n.a.	175.01	0.41	n.d.
BM-03-01; n=6	Max	n.a.	49.84	272.06	30141.73	0.76	n.a.	1139.78	2.73	1.27
	Mean	n.a.	33.17±10.81	169.9±94.36	21219.23±10349	0.42±0.2	n.a.	728.7±430.19	0.99±0.9	0.38±0.59

n.d. – not detected; n.a. – not analyzed

ACCEPTED MANUSCRIPT

Table 3. Summary of the SIMS analyses of Au and As in pyrite from orogenic gold: Golden Pond (Quebec, Canada); Kanowna Belle, Lancefield, Mickey Doolan, New Celebration, Sons of Gwalia (Australia), and Ok Tedi Cu-Au porphyry (Papua New Guinea) deposits.

Deposit	Data Points		As (wt. %)	Au (ppm)
Golden Pond	14	Min.	0.078	0.1
		Max.	0.74	4.1
		Mean ±σ	0.31±0.39	1.01±1.26
Kanowna Belle	39	Min.	0.002	0.14
		Max.	2.64	92
		Mean ±σ	0.24±0.45	10.04±12.13
Lancefield	20	Min.	0.00016	0.1
		Max.	1.62	8
		Mean ±σ	0.13±0.35	1.63±2.11
Mickey Doolan	16	Min.	0.017	0.22
		Max.	0.97	67
		Mean ±σ	0.45±0.29	18.21±21.59
New Celebration	14	Min.	0.000047	0.03
		Max.	0.0034	0.15
		Mean ±σ	0.0009±0.001	0.18±0.08
Sons of Gwalia	30	Min.	0.01	0.09
		Max.	1.04	24
		Mean ±σ	0.28±0.26	2.78±5.60
Ok Tedi	55	Min.	0.0002	0.21
		Max.	0.38	16.6
		Mean ±σ	0.04±0.071	1.98±2.94

Figure 1

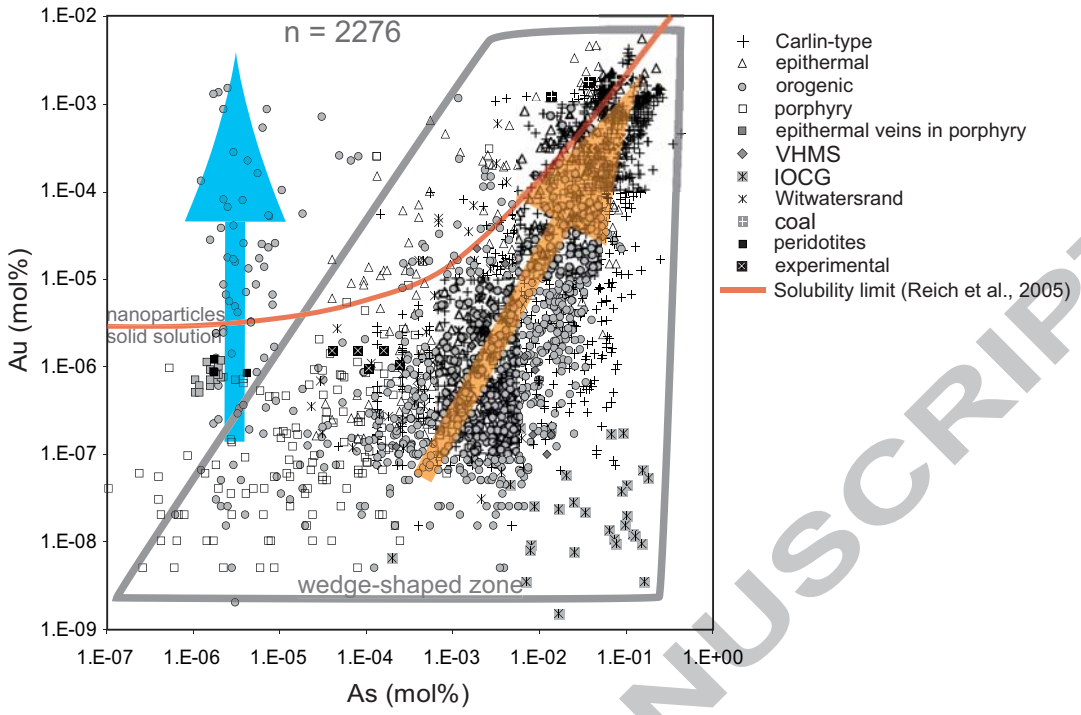

Figure 2

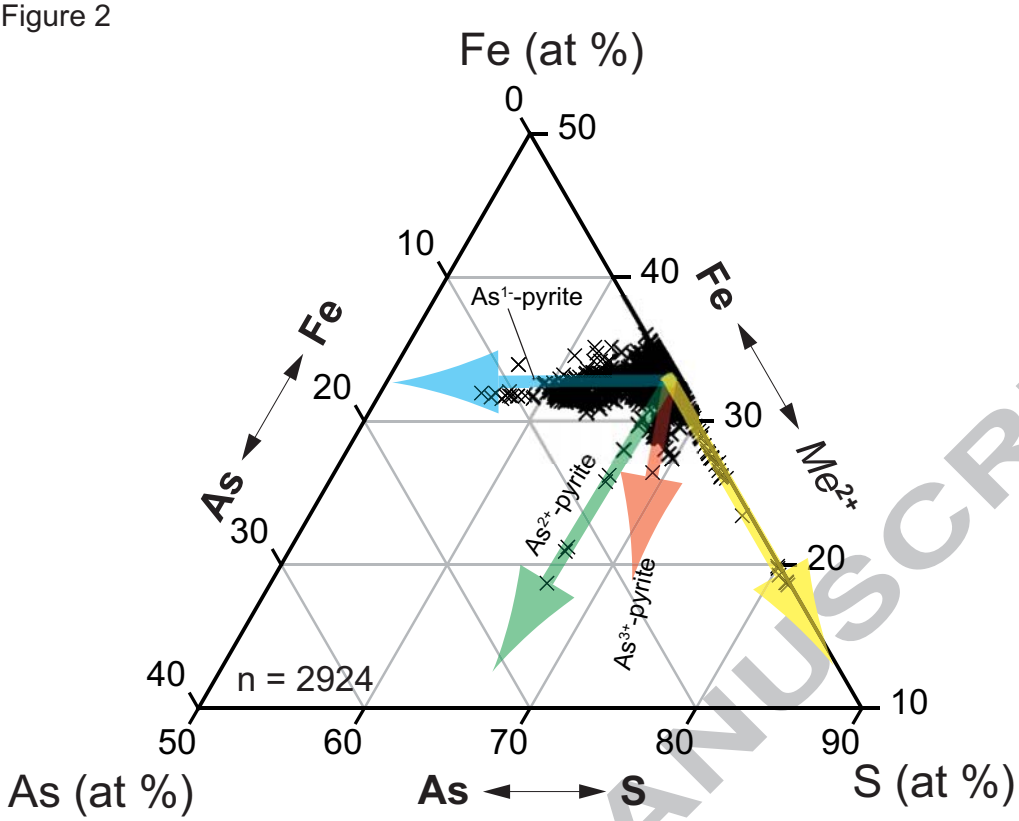

Figure 3

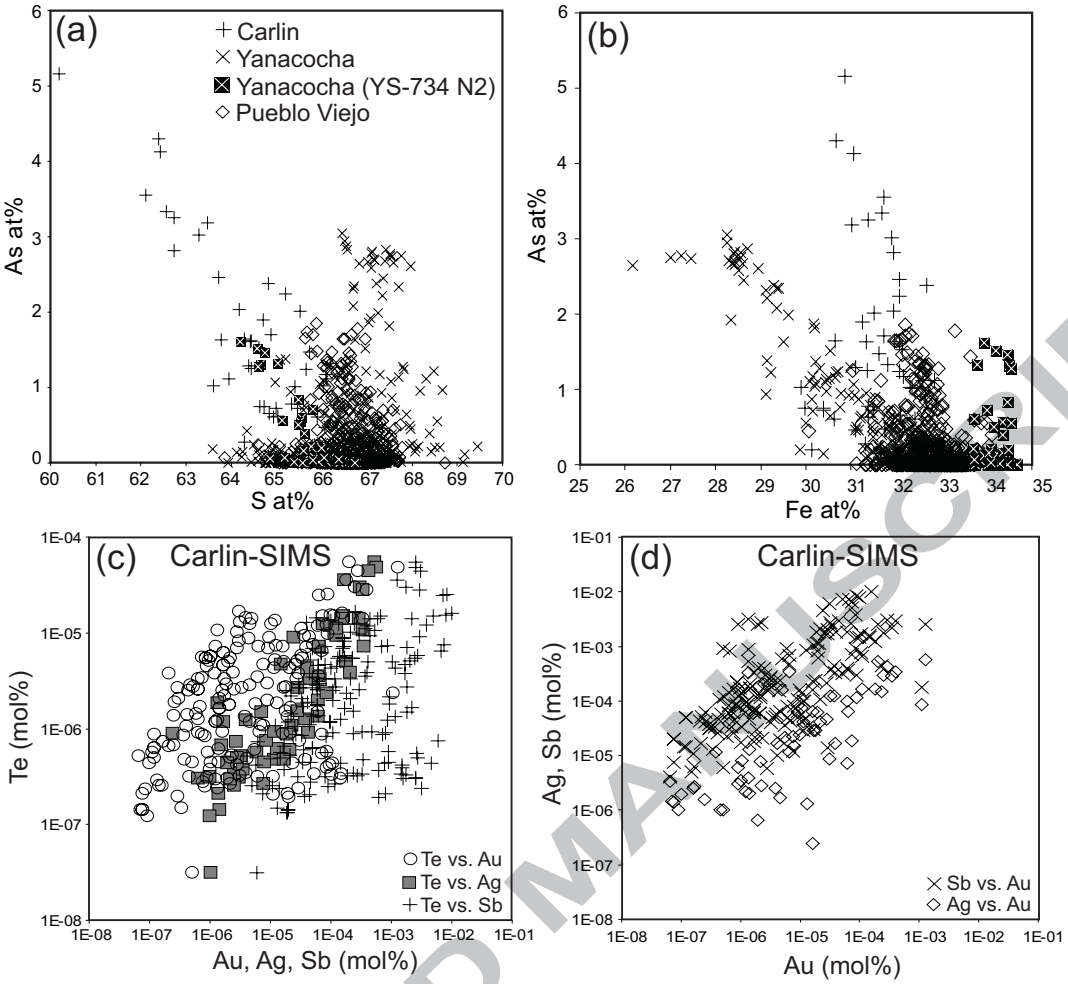

Figure 4

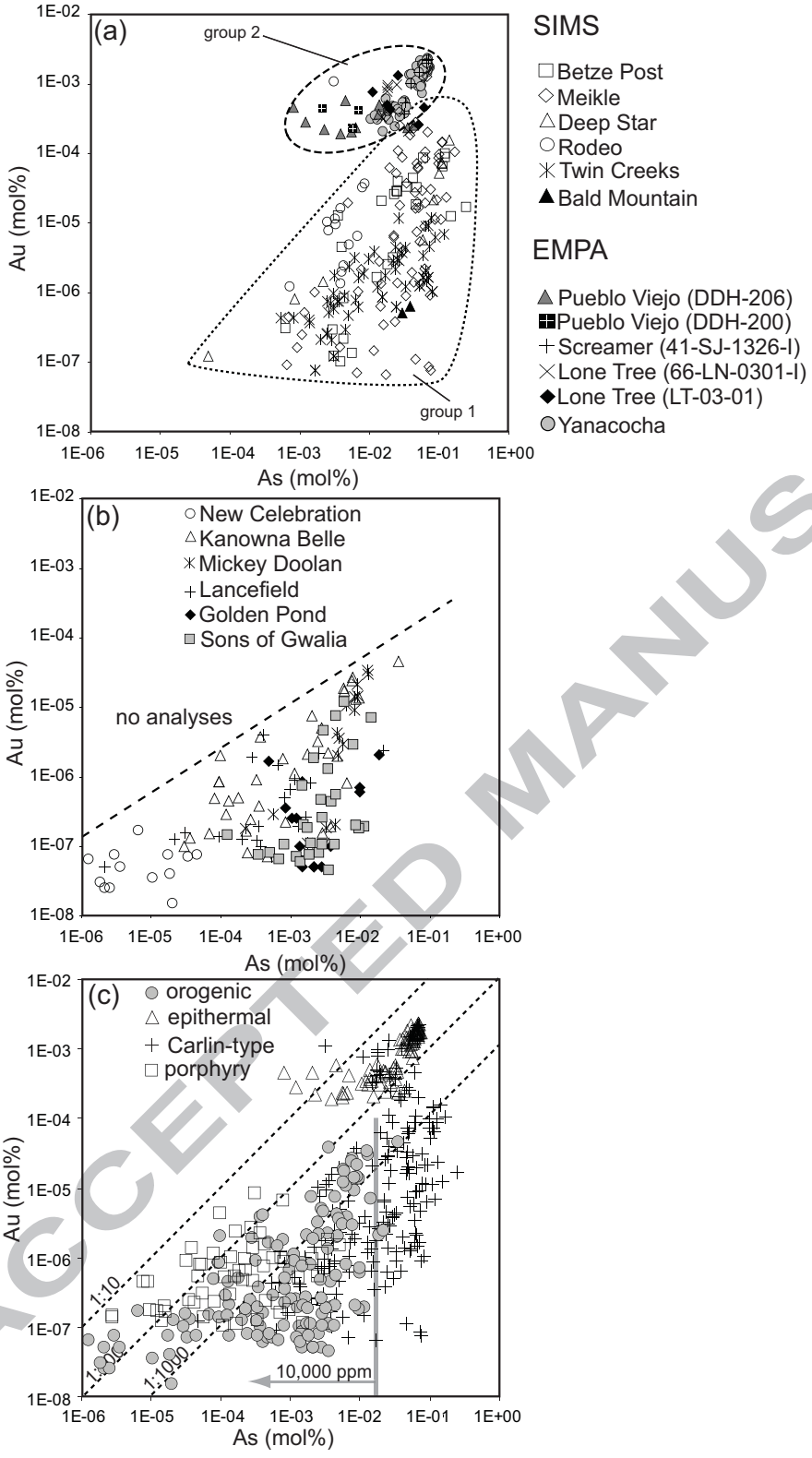

Figure 5

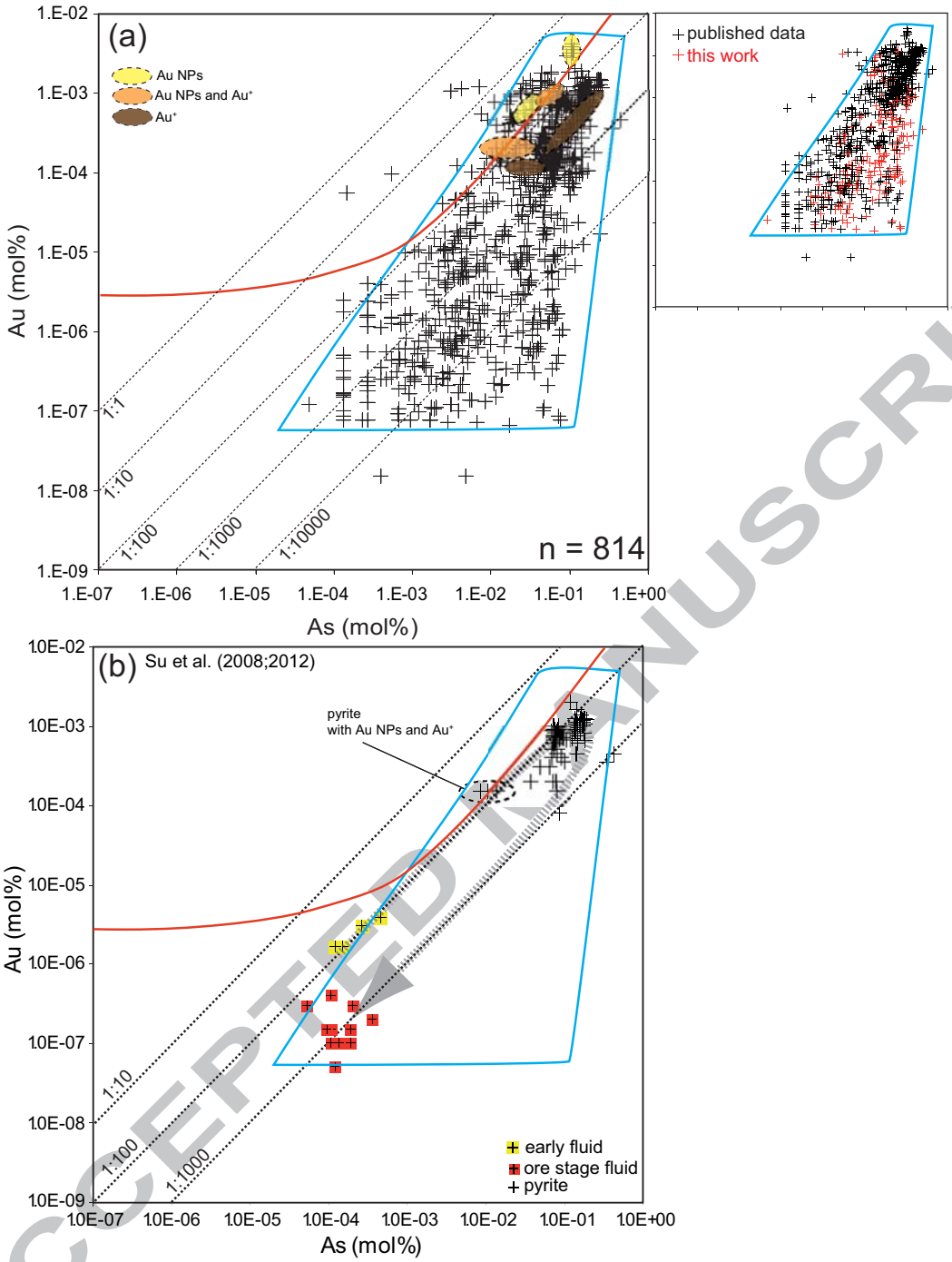

Figure 6

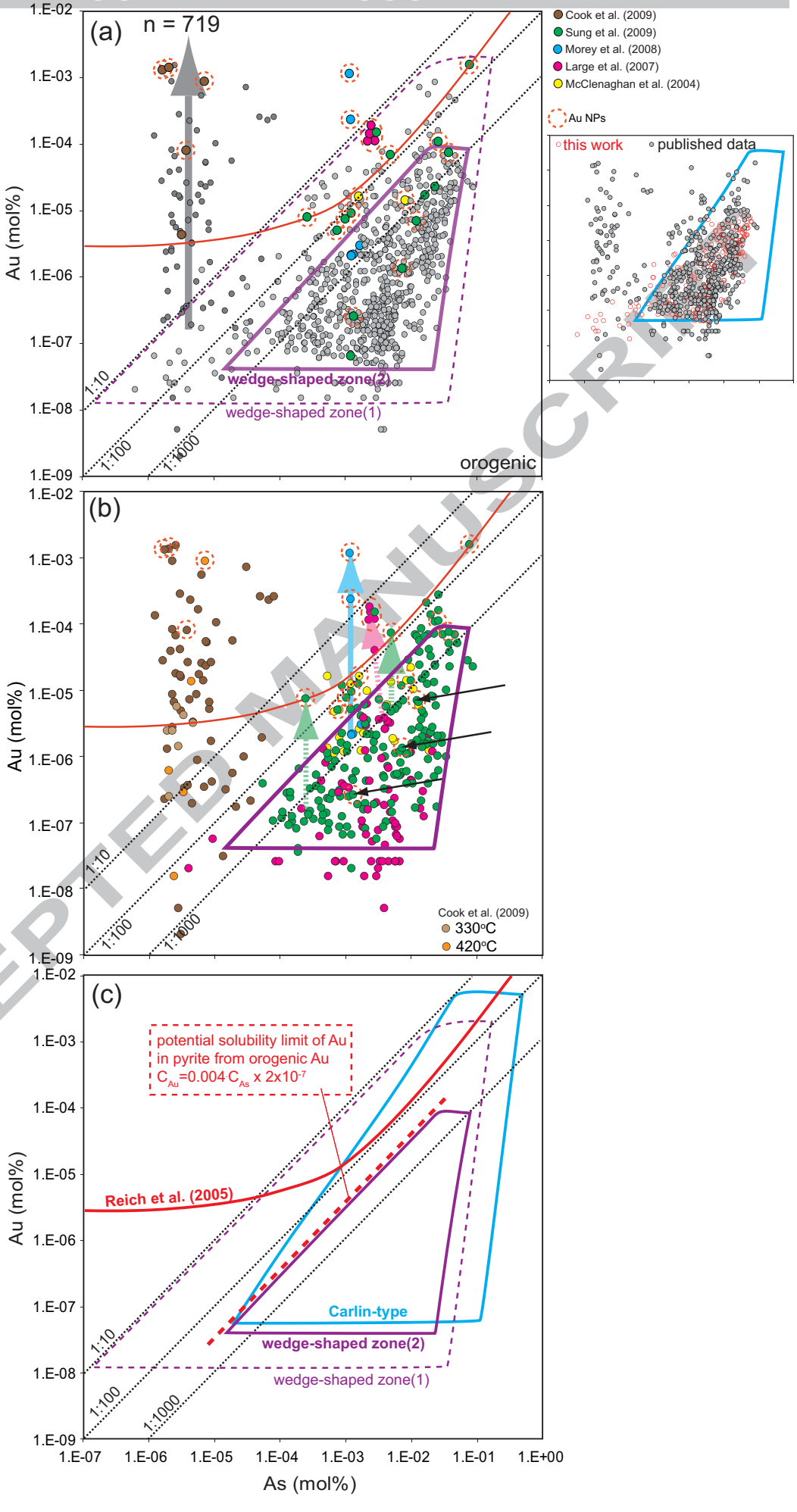

Figure 7

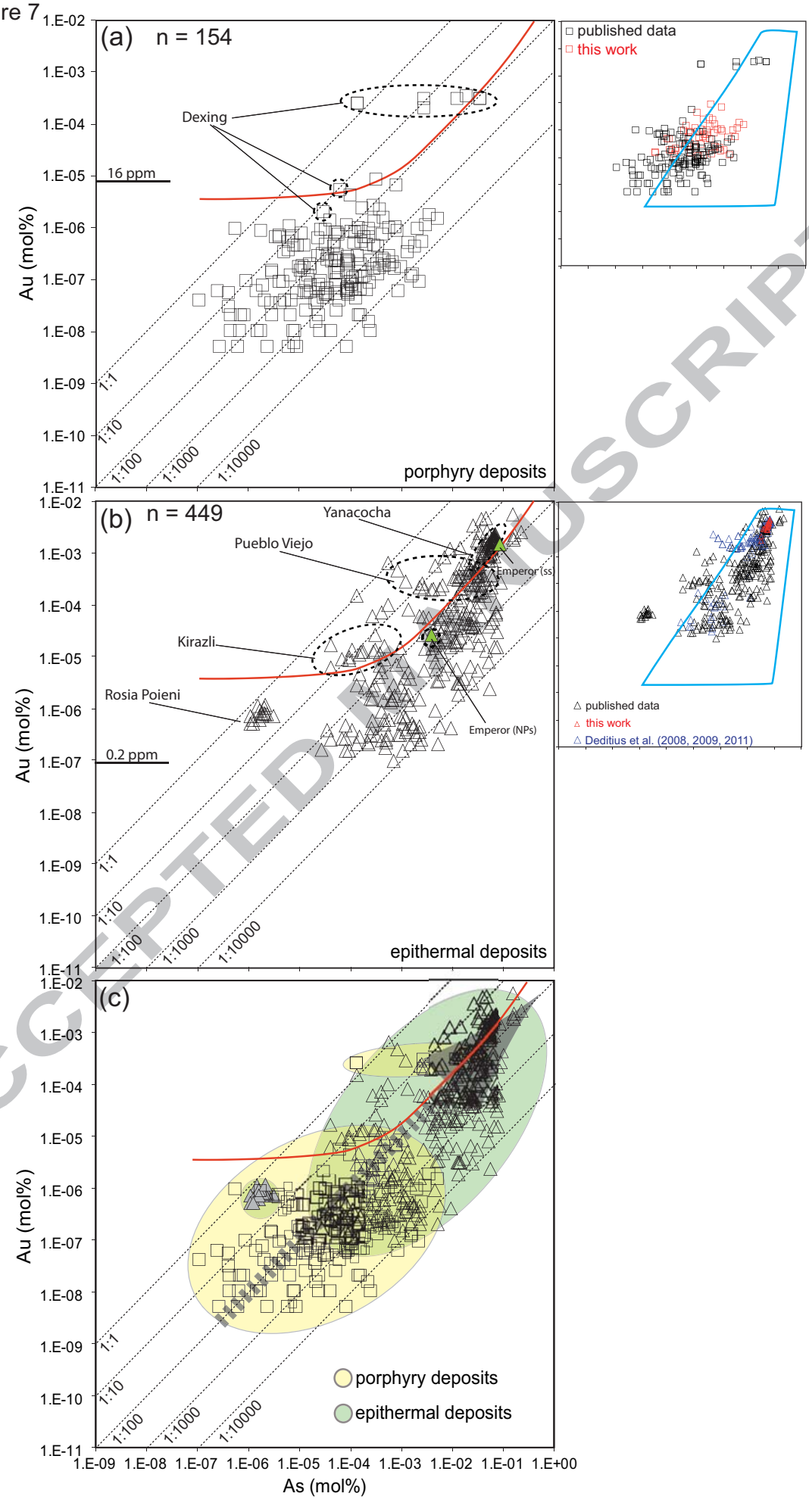

Figure 8

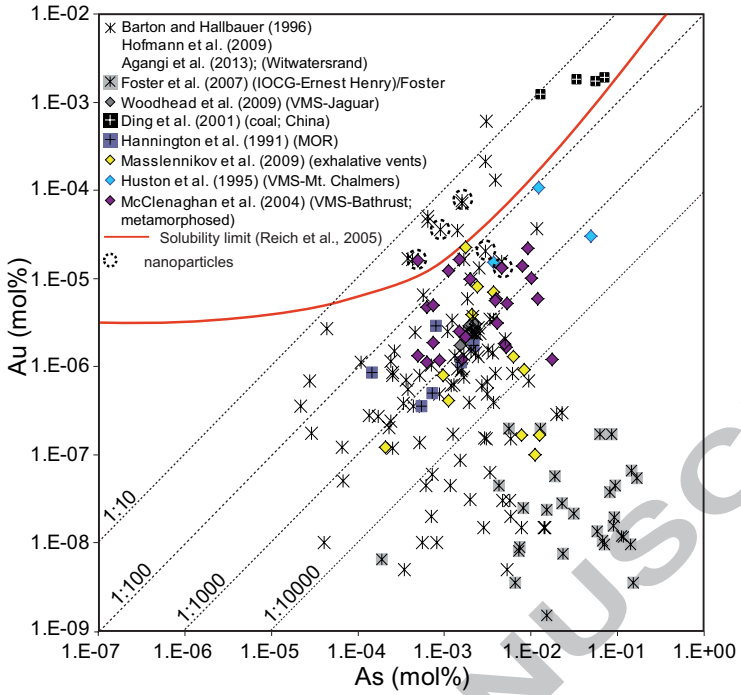

Figure 9

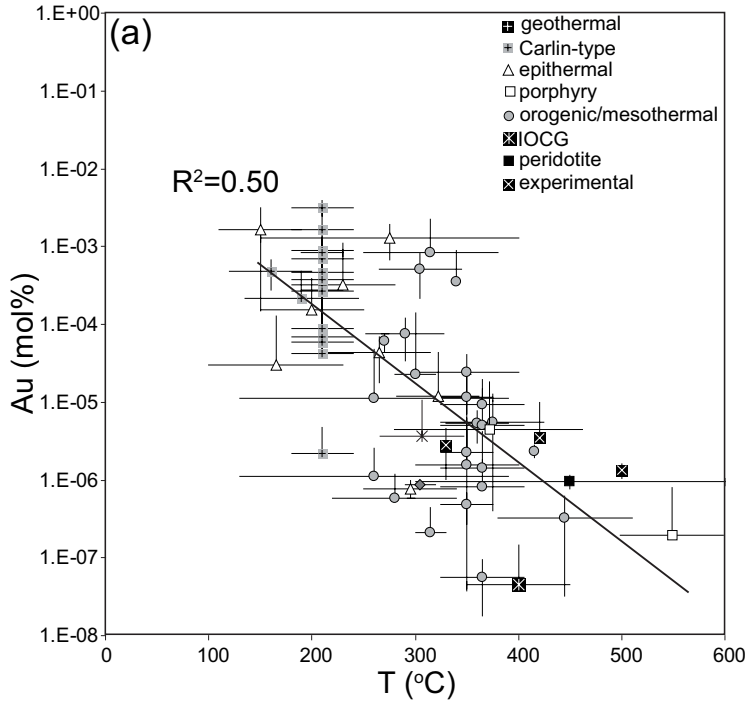

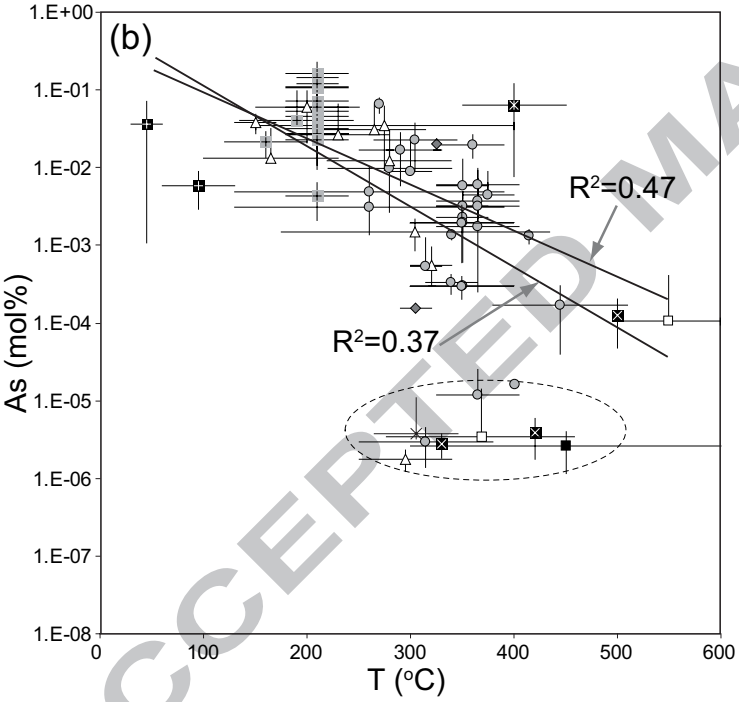

Figure 10

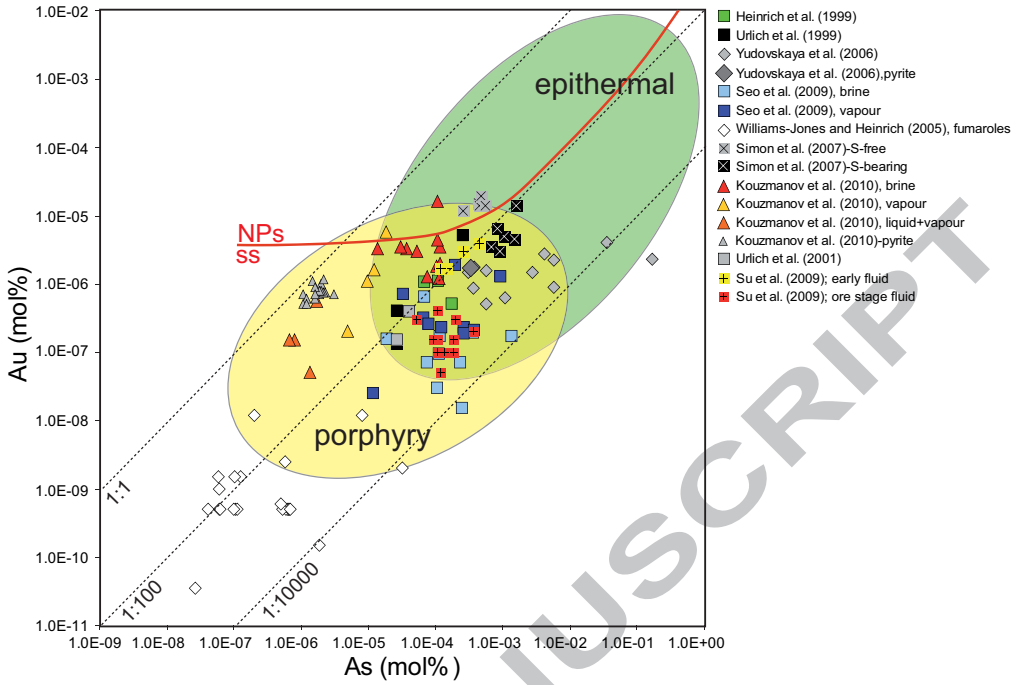

Figure 11